Henrik Elias Vatn Skaldebø

Implementing slice-wise shimming for 7T MRI

Master's thesis in Applied Physics and Mathematics
Supervisor: Johanna Vannesjö
June 2022

Master's thesis

NTNU
Norwegian University of Science and Technology
Faculty of Natural Sciences
Department of Physics

NTNU
Norwegian University of
Science and Technology

Henrik Elias Vatn Skaldebø

Implementing slice-wise shimming for 7T MRI

NTNU
Norwegian University of
Science and Technology

Abstract

To achieve high-quality images and good signal in Magnetic Resonance Imaging, the homogeneity of the static magnetic field is vital. Introducing a subject into the magnet induces distortions to the field due to local variations in magnetic susceptibility which produces image distortion and signal loss. Shimming is the method in which inhomogeneities are compensated for by using special coils that mirrors spherical harmonic functions to oppose the field. The complexity of fields one can shim is relatable to the order of spherical harmonics available. The aim of this master thesis was to develop and implement a dynamic slice-wise method on a gradient echo sequence. By updating the 1st-order shims for every slice, the compensation can possibly follow a more complex inhomogeneity than standard low-order shims. The functionality of the method was validated by running several measurements on a phantom. In vivo brain measurements of a healthy volunteer was also acquired to investigate the effect of the method. Comparisons were made between measurements with and without the method applied. The results show that slice-wise shimming can improve the signal of the brain both as a stand-alone method and as a supplement to static shimming. However, wrapping in the field map can occur and would need proper compensation to achieve good results.

Sammendrag

For å oppnå bilder av høy kvalitet og med godt signal i magnetisk resonansavbildning er homogeniteten til det statiske magnetfeltet avgjørende. Når et legeme introduseres i magneten induseres forvrengninger i feltet på grunn av lokale variasjoner i magnetisk susceptibilitet som fører til bildeforvrengning og signaltap. Shimming er en metode der inhomogeniteter er kompensert for ved å bruke spesielle spoler som speiler sfæriske harmoniske funksjoner og opponere feltet. Kompleksiteten til feltene man kan shimme er relatert til ordenen av sfæriske harmoniske som er tilgjengelig. Målet med denne masteroppgaven var å utvikle og implementere en dynamisk, snittvis metode på en gradient echo sekvens. Ved å oppdatere 1. ordens shims hvert snitt, kan kompensasjonen muligens følge en mer kompleks inhomogenitet enn standard lavordens shims. Funksjonaliteten til metoden ble validert ved å kjøre flere målinger på et fantom. For å undersøke effekten, ble in vivo målinger av hjernen til en frisk frivillig tatt. Det ble gjort sammenligninger mellom målinger med og uten metoden anvendt. Resultatene viser at snittvis shimming kan forbedre signalet til hjernen både som en frittstående metode og som et supplement til statisk shimming. Allikevel kan vrengninger i feltkartet oppstå og passende kompensasjon er nødvendig for å oppnå gode resultater.

Acknowledgements

This master's thesis is a culmination of my final two semesters at the Norwegian University of Science and Technology. I would like to extend my gratitude to my supervisor Prof. Johanna Vannesjö for giving me the opportunity to work on this project. Thank you for your guidance and patience as well as the many hours at the MRI scanner. I would also like to thank my family for their support over the years, whether it be helping me move from place to place or offering advice and experience. Finally, a thank you to all my friends who have made these five years a whole lot easier.

Contents

1 Introduction

Magnetic Resonance Imaging (MRI) utilizes the physical phenomenon of magnetic resonance to achieve images of human anatomy with superior soft-tissue contrast compared to other imaging techniques[1]. A large magnet generates a strong, static field in which the subject is placed. With radiowaves, the hydrogen nuclei in the body are excited and a signal is acquired. With gradient coils, the spatial localization of the signal is then converted into an image. A caveat, however, is that MRI is a fairly sensitive method and the homogeneity of the static magnetic field will have a large impact on the image quality. Field inhomogeneity can result in image distortion and signal loss[2]. The main source of inhomogeneities comes from the image subject itself where variations in magnetic susceptibility between tissue types induce a disruption to the static field. The process of compensating for these inhomogeneities is called shimming. The standard approach of shimming has long been to decompose the field into spherical harmonics (SH) and use shim coils mirroring the SH functions to counter the inhomogeneities. However, for small and/or complex regions of interest (ROI), lower-order SH are often not sufficient enough. Additionally, spatial and engineering restrictions limit the number of shim coils a system can include.

An alternative method to improve the shimming in complex regions is called *dynamic slice-wise* shimming. The premise of this method is to limit the problem to each separate slice at a time. The inhomogeneity within each slice is closer to a linear problem and by dynamically altering the 1st-order shims for every slice, more complex fields can be compensated. While 3T scanners, which denote the strength of the static field, have been the golden standard for MRI, the emergence of ultra-high field (UHF) 7T scanners can provide even higher quality imaging as the signal-to-noise ratio (SNR) and spatial resolution can increase[3]. However, so do the induced magnetic field inhomogeneities and shimming is therefore increasingly vital when moving to higher-field scanners.

Previous studies have shown that dynamic shimming can improve image quality in several aspects. Juchem et. al. (2010) showed that a dynamic shim update (DSU) approach of zero- through third-order shims improves on the standard shim coil system and provides better homogeneity overall in 7T imaging[2]. In 2012, Finsterbusch et. al. used slice-specific z-shim gradient pulses to improve T2*-weighted imaging of the spinal cord[4]. Several measurements at 3T showed an increase in signal intensity and a decrease in signal variation which was deemed beneficial for fMRI in the spinal cord.

The aim of this master thesis was to implement a slice-wise shimming method on the 7T MRI scanner at St. Olavs Hospital in Trondheim, the Siemens MAGNETOM Terra System. The work is a continuation of the specialization project from the fall of 2021 which studied a calculation method to determine slice-specific shim values[5]. The specific goals to be achieved in this master's thesis were:

1. Expand the gradient echo (GRE) sequence from Siemens to include slice-wise shimming.

2. Work out a pipeline for calculations and measurements with slice-wise shimming.

3. Use phantom measurements to investigate and validate the method.

4. Make in vivo measurements of the brain with slice-wise shimming and evaluate the results.

2 Theory

The following chapter will aim to provide a general overview of the theory relevant to this thesis. This includes the magnetic resonance phenomenon, imaging sequences, spatial encoding, B_0 inhomogeneity and shimming. Note that some of the theory in this chapter is based on the preceeding project thesis[5].

2.1 Magnetic Resonance

The foundation of the MRI method is based on the physical phenomenon of Nuclear Magnetic Resonance (NMR). This is an interaction that occurs between an external magnetic field and nuclei with a magnetic moment[6]. An electromagnetic wave with a certain frequency matching the nuclei can excite it to a higher energy state. When the nuclei relax back to their original state, the fluctuation is possible to be observed as a specific electromagnetic signal. As the hydrogen atom is the most abundant in human biology, it is the standard atom to image[1]. Due to this, MRI provides better soft-tissue contrast, e.g. in the brain, than other imaging methods like CT and PET. And as MRI only uses magnetic fields up to radio frequencies, compared to higher frequency radiation in CT and PET, MRI is seen as a non-invasive method.
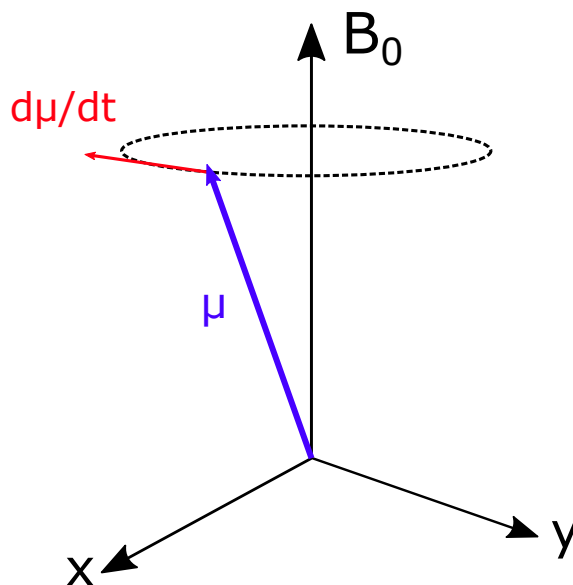

Figure 2.1: The z-axis in MRI is defined as the direction of the static magnetic field, B_0. The magnetic moment, μ, will precess around B_0 in the dotted line due to the torque. The magnitude of the change stays constant, but its orientation will vary.

2.1.1 Properties of the nuclei

To properly understand the fundamentals of MRI, some quantum mechanics is needed. In particular, the spin magnetic moment which is a property of elementary particles which results from their spin. A conventional hydrogen atom has one proton, which possesses the spin property, in addition to neutrons and whole nuclei. In the case of the hydrogen atom, we can simply concentrate on the proton as that is the whole nucleus. The spin can be related to the classical property of the angular momentum, L, of an object in a circular trajectory. And in electromagnetism, this is also relatable to when a current travels through a loop inducing a magnetic moment, μ. The term "spin" and "magnetic moment" is often used interchangeably in MRI. However, a particle with spin is not actually spinning or rotating. Spin is an intrinsic, quantized property and in comparison to the angular momentum, it interacts with a magnetic field, not a gravitational field. The electromagnetic moment of a nucleus is proportional to the angular momentum and a constant factor called the gyromagnetic ratio, γ[6], and is written as

$$\mu = L\gamma. \tag{2.1}$$

Similar to how mass in circular motion experiences a torque, τ, because of gravity, so does the magnetic moment in a magnetic field. The torque for a magnetic moment is then

$$\tau = \mu \times B_0, \tag{2.2}$$

where B_0 is a static magnetic field. With Newton's second law, the torque can be written as $\tau = dL/dt$. Combining this with the previous equations shows how the change in the magnetic moment is related to the magnetic moment itself and the magnetic field. Figure 2.1 and Equation 2.3 shows this relation. Note as well that since the change in the magnetic moment is orthogonal to the magnetic moment itself and the magnetic field, $d\mu/dt \perp \mu, B_0$, it can only change direction, not magnitude.

$$\frac{d\mu}{dt} = \gamma\mu \times B_0. \tag{2.3}$$

Equation 2.3 shows how the magnetic moment behaves when it is not parallel to the magnetic field. It will experience a change in its direction that is perpendicular to both the magnetic moment and the magnetic field. This results in a precessional motion around the direction of the magnetic field. Solving the cross product of the equations, assuming that B_0 is in the z-direction, shows that the precession indeed only happens in the x- and y-directions as predicted by the dotted line in Figure 2.1. The frequency at which the magnetic moment precesses is γB_0 and is called the *Larmor* frequency, ω_0. This frequency is given by the following equation, called the Larmor equation,

$$\omega_0 = \gamma B_0. \tag{2.4}$$

As mentioned, we need a certain frequency to excite the nuclei. This is the Larmor frequency and we can excite the nuclei if we know their gyromagnetic ratio as we control the magnitude of the magnetic field ourselves. The gyromagnetic ratio is commonly given as MHz/T, and for hydrogen this is $\gamma = 42.573$ MHz/T[6].

2.1.2 Magnetization

Without any outside interference, the magnetic moments of the hydrogen nuclei are randomly oriented. By placing them in a magnetic field, the nuclei are focused and aligned with the external field. It was previously mentioned that spin is a quantized property. The number of spin states can be determined using the equation for the number of energy states[1],

$$N = 2S + 1. \tag{2.5}$$

S is the spin quantum number and in the case of the hydrogen $S = 1/2$. Thus there are two spin states for the hydrogen nuclei which are referred to as spin-up and spin-down. Nuclei that are of lower energy and can not oppose the magnetic field have their magnetic moment aligned parallel and spin-up to the field. Contrary, higher energy nuclei have enough energy to oppose and align themselves anti-parallel (spin-down). This is known as the Zeeman effect and makes it possible to show that for a volume, the number of parallel spins within will slightly outnumber the anti-parallel spins, and one can figure out by how much[1, 6].

Figure 2.2 shows the two spin states in a magnetic field. The energy in each state is

$$E = -\mu B_0 = -m\gamma\hbar B_0, \tag{2.6}$$

where m is the quantum number and $\hbar$ is the reduced Planck constant. In MRI the static magnetic field B_0 is commonly along the z-axis in a cartesian coordinate system. The two spin states of $1/2$ are either aligned with or against the magnetic field, so $m = \pm 1/2$. The energy difference between the lower and higher spin state is the Zeeman equation,

$$\Delta E = \gamma\hbar B_0. \tag{2.7}$$

With this equation, the distribution of spins at thermal equilibrium can be estimated using the Boltzmann equation (2.8). This relation shows how the strength of the magnetic field is proportional to the energy difference and in turn will influence the distribution of spins in the two states. A higher value for B_0 means the spins require more energy to be anti-parallel and thus the distribution becomes more biased towards parallel spins.

$$\frac{N^x}{N^-} = exp(\Delta E/kT) = exp[\gamma\hbar B_0/kT]. \tag{2.8}$$

The Boltzmann equation shows that the sum of all the spins in a given assortment will align with B_0. The net magnetic moment from this assortment is called the Net Magnetic Vector (NMV) or just the magnetization vector M[1]. This simplifies the quantum mechanical nature of the spins and the magnetization vector follows classical physics. The size of this vector is then directly related to the strength of the magnetic field. Increasing B_0 would increase M. The results of the Boltzmann equation also show how sensitive MRI is. With a standard 3T magnetic field strength, there are only about 10 parallel nuclei in excess per million.

When aligned with the magnetic field the magnetic moment will precess around B_0 as in Figure 2.1. The net magnetization vector consists of a multitude of these moments and as a result, will cancel out each other's transversal components. Figure 2.3 shows how at the thermal equilibrium the excess of parallel spins will therefore create the magnetization vector in the same direction as B_0.
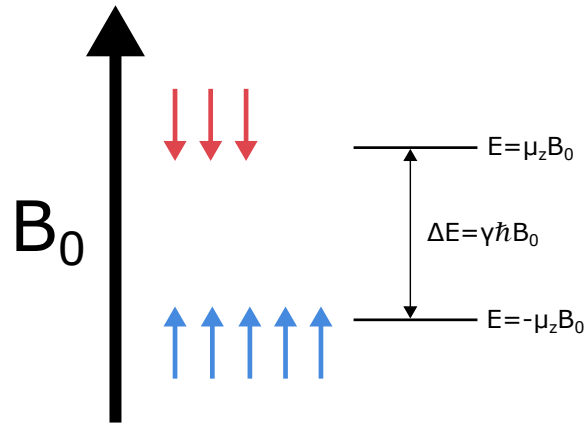
Figure 2.2: Spins aligned (parallel) with the magnetic field are low-energy nuclei, while anti-parallel spins have enough energy to oppose the magnetic field and are high-energy nuclei. The energy difference between the two spin states results in the Zeeman equation.

Laboratory versus rotational frame   When introducing more than one spin, the precession quickly makes it confusing to visualize our case in a laboratory frame. To solve this we can imagine the frame rotating at the same frequency as the spins precess at. This results in all resonating spins appearing to stand still, while off-resonance spins will precess according to their frequency difference. Figure 2.4 illustrates the rotating frame.

2.1.3 The MR signal

To achieve a signal, the system has to be perturbed[1, 6]. A radio frequency (RF) pulse, often denoted as B_1, is used to tip the spins down to the transversal plane. It is in this plane the signal is measured. Since the spins are aligned with the static magnetic field in a low energy state, energy needs to be transferred to the spins for them to be seen in the transversal plane. Resonance is the phenomenon where an oscillation with a certain frequency can transfer energy to an object with a similar natural frequency. The RF pulse therefore needs to have the same frequency as the Larmor frequency of the hydrogen nuclei. If the RF pulse were to be applied with a completely different frequency, the nuclei simply would not be energized. The strength and duration at which the RF pulse is applied also determine the flip angle. This is the angle at which the NMV is tipped. The most common example is as in Figure 2.5 where the flip angle is 90° and the NMV is fully in the transversal plane, but we can freely choose the angle according to our needs.

The Free Induction Decay   Now that the NMV is precessing around B_0 in the transversal plane, a signal can be measured using Faraday's law of induction and a receiving coil[1]. This law explains how the change in magnetic flux within a closed circuit produces an electromagnetic force (emf). For a tightly wound coil with N turns the emf is

$$\epsilon = -N\frac{d\Phi}{dt},\tag{2.9}$$

where ϵ is the emf and Φ is the magnetic flux. Because of Lenz's law, the emf will oppose the magnetic field, hence the negative sign[1]. The measured signal is the induced current which is carried by the emf. As the NMV precesses, the signal will therefore follow a
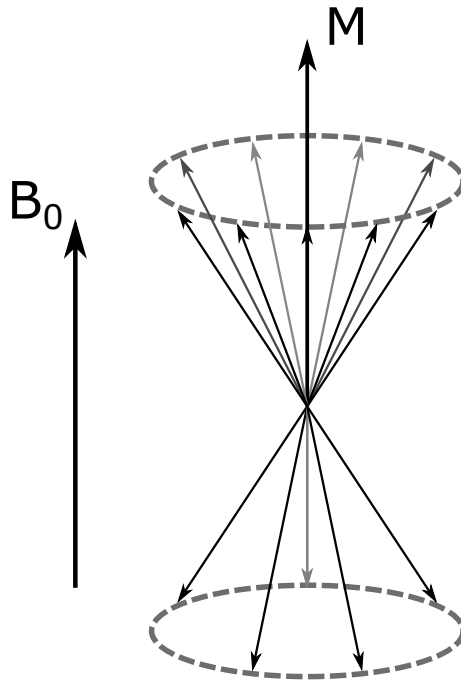
Figure 2.3: At thermal equilibrium, the parallel spins in a certain volume slightly outnumber the anti-parallel spins. The transversal components cancel out and the magnetization vector M becomes a sum of the longitudinal components.

sinusoidal pattern which will follow the precessional frequency. However, when the RF pulse is over, the system will lose energy and return to equilibrium. This means that the signal will gradually lose strength as the NMV aligns itself with B_0 again. This is the most basic MR signal called the free induction decay (FID) signal and is illustrated in Figure 2.6.

2.1.4 Relaxation

Fundamental thermodynamics states that a system will seek to return to its equilibrium, or its lowest energy state[1, 7]. The process in which the system in MRI loses energy and the signal gradually decreases is called relaxation and happens after the application of the RF pulse. There are two components to the relaxation process. The most apparent, where the absorbed RF energy is released and the magnetization vector aligns itself with B_0 again, is referred to as T1 recovery or longitudinal relaxation. Initially, the spins are all in phase after the excitation tips them to the transversal plane. The second component of relaxation stems from the magnetic moments of the nuclei losing their phase coherence and in turn diminishing the transversal component of the magnetization vector. This is referred to as T2 decay or transversal relaxation.

A helpful tool to understand relaxation is the Bloch equations which describe how the components of the magnetization vector evolve over time. Equation 2.10 and 2.11 describes the transverse components, M_x and M_y, while Equation 2.12 describes the longitudinal component, M_z[6]. The time, t, refers to the period after the RF pulse is applied, while M_0 is the initial value for the magnetization vector, before the RF pulse. The equations also contain the two variables, T1 and T2, which are intrinsic properties of a tissue describing the two types of relaxation.
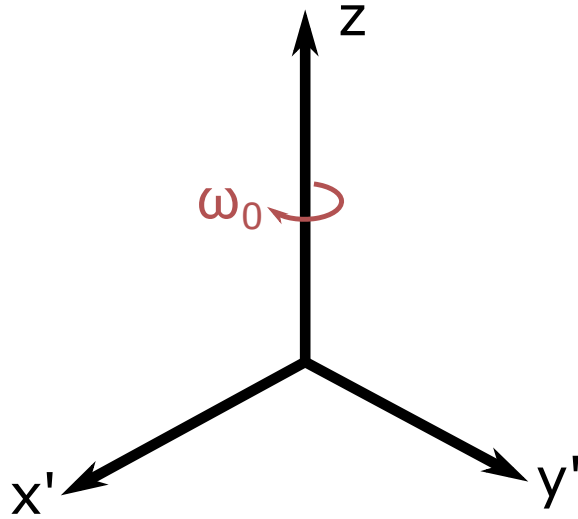
Figure 2.4: By rotating the laboratory frame around the z-axis with the same frequency as the Larmor frequency, a new rotating frame is achieved. The new frame is recognized by the marked coordinates x' and y'.

$$\frac{dM_x(t)}{dt} = \gamma(M(t) \times B(t))_x - \frac{M_x(t)}{T2}. \tag{2.10}$$

$$\frac{dM_y(t)}{dt} = \gamma(M(t) \times B(t))_y - \frac{M_y(t)}{T2}. \tag{2.11}$$

$$\frac{dM_z(t)}{dt} = \gamma(M(t) \times B(t))_z - \frac{M_z(t) - M_0}{T1}. \tag{2.12}$$

Longitudinal relaxation The released energy from the nuclei in longitudinal relaxation is dispersed to the surroundings, or the molecular lattice, which is why this type of relaxation is also called spin-lattice relaxation[7]. The third Bloch equation can be reduced as $(M(t) \times B(t))_z = 0$ since $B(t) = (0, 0, B_0)$ assuming no resonant RF field is applied.

$$\frac{dM_z(t)}{dt} = \frac{1}{T1}(M_0 - M_z(t)). \tag{2.13}$$

Solving the differential equation with the initial condition $M_z(0) = 0$ gives

$$M_z(t) = M_0(1 - e^{-t/T1}). \tag{2.14}$$

This equation dictates that at t=T1, the longitudinal component will have reached 63% of its maximum value.

Longitudinal relaxation also has a say in the choice of flip angle. To maximize the signal for a measurement, the Ernst angle is the most optimal angle[1, 6]. This angle is given as a relationship between the relaxation time T1 and the repetition time TR, which is the time between successive excitations of the same spins. The Ernst equation 2.15 gives the angle providing the highest SNR for a certain repetition time:
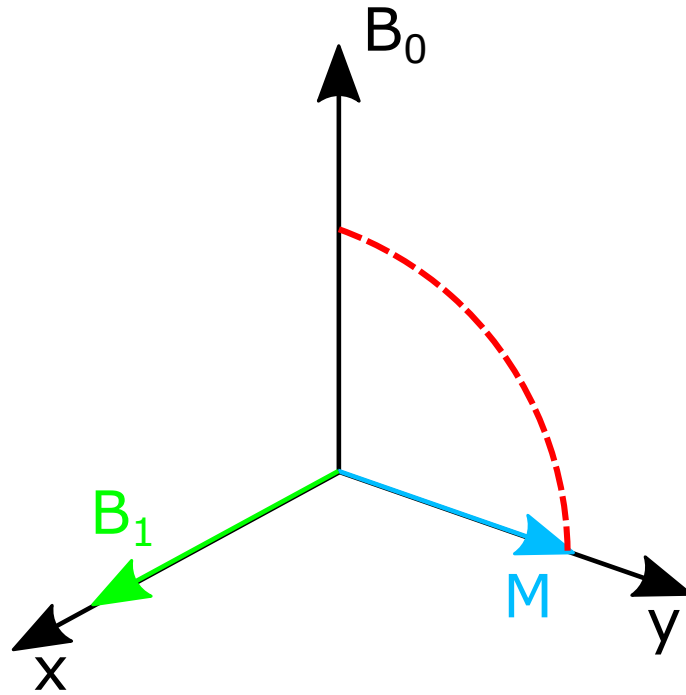
Figure 2.5: A 90° RF pulse (B_1) tips the magnetization vector down to the transversal plane.

$$\Theta_E = \arccos\left(e^{-\frac{TR}{T1}}\right). \tag{2.15}$$

Transversal relaxation   Simultaneously as the T1 recovery, there is also a loss of coherence among the nuclei called T2 decay. This is mainly due to dipole-dipole interactions where the magnetic fields of neighbouring hydrogen nuclei interact with each other. Remember from Figure 2.3 that not all spins are pointing directly in the same direction as the magnetization vector. After the RF pulse, the spins will precess within the plane. Spins that were aligned with B_0 will create a slightly larger magnetic field than the neighbouring spins experience which were oppositely aligned with B_0. The resulting precessional frequency of these spins would in this case increase. The opposite case can also be applied to spins that were oppositely aligned with B_0 and the frequency will be lower[1]. Additionally interactions between neighbouring spins can lead to energy transfer similar to how spin-lattice relaxation worked. These cases are referred to as spin-spin interactions and the small changes in frequency and energy is enough to cause dephasing of the magnetic moments in the spins. The result of this dephasing is that the total sum of the magnetization vector decreases since it is less focused.

Another source of dephasing is caused by inhomogeneities in the magnetic field. The variations in the magnetic field leads to changes in the precessional frequency individual spins. Spins that lie in areas with higher field strength will have their frequency increased, while for the spins in lower fields it will decrease.

The first and second Bloch equations can be combined and reduced to Equation 2.16.
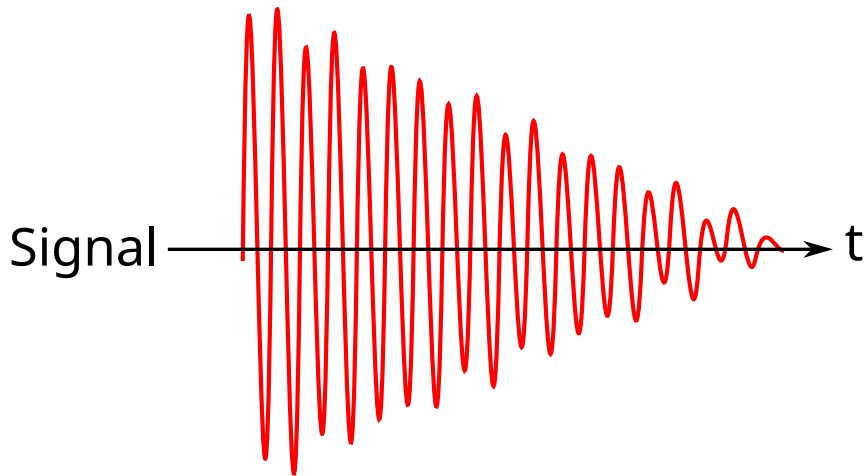
Figure 2.6: The free induction decay signal oscillates and decreases over time as the system returns to equilibrium.

$$\frac{dM_{xy}(t)}{dt} = -\frac{1}{T2}M_{xy}(t).$$ (2.16)

Solving the differential equation with the initial condition that the transverse magnetization is $M_{xy}(0)$ at $t = 0$. In the case of the $90°$ pulse, this would be the same length as M_0.

$$M_{xy}(t) = M_{xy}(0)e^{-t/T2} = M_0e^{-t/T2}.$$ (2.17)

This equation shows that at t=T2, the transverse magnetization has decayed to about 37% of its initial value. The echo time (TE) is the time interval between the RF pulse and when the signal is acquired by the receiving coil. Determining the length of this interval will impact how much T2 decay occurs before signal readout.

Since T2 is an intrinsic quality of the tissue, one might expect that in reality, the decay is faster because of the dephasing due to the field inhogoneities which are external. This is actually the case and the true, or observed, T2 is referred to as T2*. This value is always less than or equal to T2. The decay stemming from inhomogeneities is referred to as T2' and Equation 2.18 shows the relation between the three variables,

$$\frac{1}{T2*} = \frac{1}{T2} + \frac{1}{T2'}.$$ (2.18)

T2' is known as a reversible process. As long as the inhomogeneities are constant for the relevant spins, "flipping" them with a $180°$ pulse will reverse the dephasing.

2.2 Imaging sequences

An image sequence is a timed process where the MRI system applies RF pulses and gradients[1]. It is common that a sequence has a specific series of pulses that are repeated before a new RF pulse excites the subject again. Each repetition has small variations which

makes it possible to image the whole subject. The length of this repetition is referred to as the repetition time, TR, which is the same used in the Bloch equations. The FID which was introduced earlier is fairly short which makes it difficult to measure. Imaging sequences therefore uses different techniques to revive the signal as an echo. The point of this echo is at the echo time, TE.

The contrast and result of the image can be weighted and manipulated by determining TE and TR. E.g. with a shorter TR than T1 of a tissue, the tissue will not fully recover before the next RF pulse. Contrast in the image will then be more pronounced between tissues with short T1, which fully recover their magnetization vector, and tissues with long T1 who do not.

2.2.1 Gradient Echo

One of the most basic sequences is the gradient echo sequence[1]. Each repetition starts with the RF pulse and a gradient in the slice-direction which is called the slice-selective pulse and can be seen in Figure 2.9 which shows one repetition. The purpose of this gradient is to change the resonance frequency of the subject, usually along the z-axis. Additionally, a slice select rephasing gradient is applied to minimize phase dispersion after in the transverse plane due to the slice-selective pulse. The frequency of the RF pulse can then be set to only excite one specific slice of the subject by including the frequency offset. Figure 2.7 visualizes this concept.
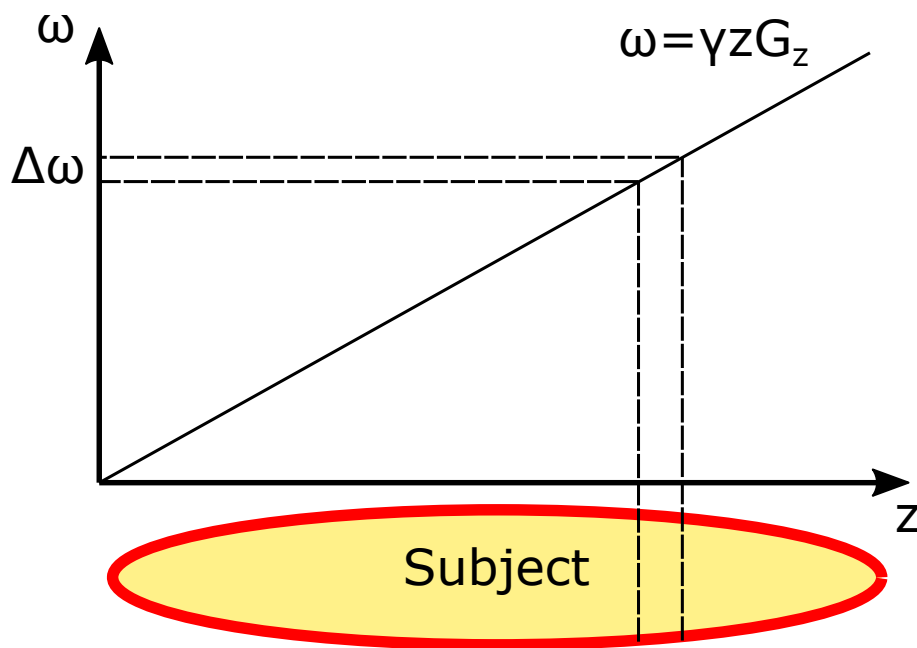
Figure 2.7: The gradient along z increases the magnetic field dependent on the position. This change results in a frequency offset, ω. The RF pulse uses this offset to only excite the corresponding slice. Note that the thickness of the slice depends on the bandwidth of the frequency offset, $\Delta\omega$, and the steepness of the gradient.

The phase selection is usually applied in the y-direction. Note that in Figure 2.9 this is visualized as several rectangles stacked upon each other. This is to indicate that the value and polarity vary for each repetition. The strength of this gradient determines the phase of the nuclei in the slice and will be further discussed in the following section.

In the frequency direction, usually the x-axis, there are two pulse objects. The first is the dephasing gradient which accelerates the dephasing of the FID. Next, a rephasing gradient is applied with the same strength, but opposite polarity. This gradient refocuses the spins that were initially dephased and the resulting echo is measured. During this echo, a receiving coil is also active and measuring the signal.

Figure 2.8: The signal from the FID is resurrected as an echo after rephasing.

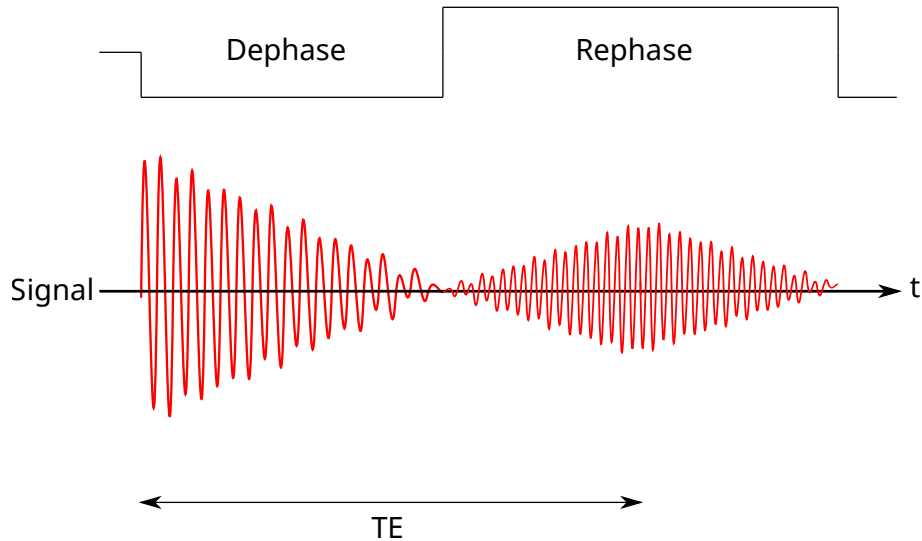Another common imaging sequence is the spin echo[1]. The main difference between the two is that the spin-echo sequence uses two RF pulses instead of one. The second RF pulse is 180° and "flips" the spins, reversing the T2*-decay. To achieve this and still maintain transversal magnetization, the initial flip angle has to be fairly large. Both the echo time and repetition time of this sequence are therefore relatively large. By using low flip angles in gradient echo, a much more rapid acquisition is achieved.

2.3 Spatial encoding

The goal of spatial encoding is to convert the echo signal into a 3D image by calculating the amount of signal from each voxel[1, 6]. In the image sequence, a slice-selective gradient reduces the scope to one slice. The remaining two gradients then determine the position and intensity of each signal within the slice.

The echo of the signal is acquired through the receiving coil as a time signal with varying current. However, this signal comes from all the voxels in the excited slice. To distinguish the signal it is decomposed using the Fourier transformation which is a mathematical technique converting the signal from the time domain to the frequency domain[6]. It allows us to look at the time signal as a sum of sine waves with different frequencies, phases and amplitudes. Figure 2.10 is a visual representation of how a time signal $s(t)$ is Fourier transformed into a frequency signal $S(\omega)$.

In MRI, the frequency data is organized in what is called k-space which is a matrix of numbers representing spatial frequencies in an image slice. Each point in k-space is not a one-to-one analogue to each pixel in the image. However, each point in k-space contains information about that specific spatial frequency in every pixel in the image. And vice versa each pixel in the image contains information from every point in k-space. The
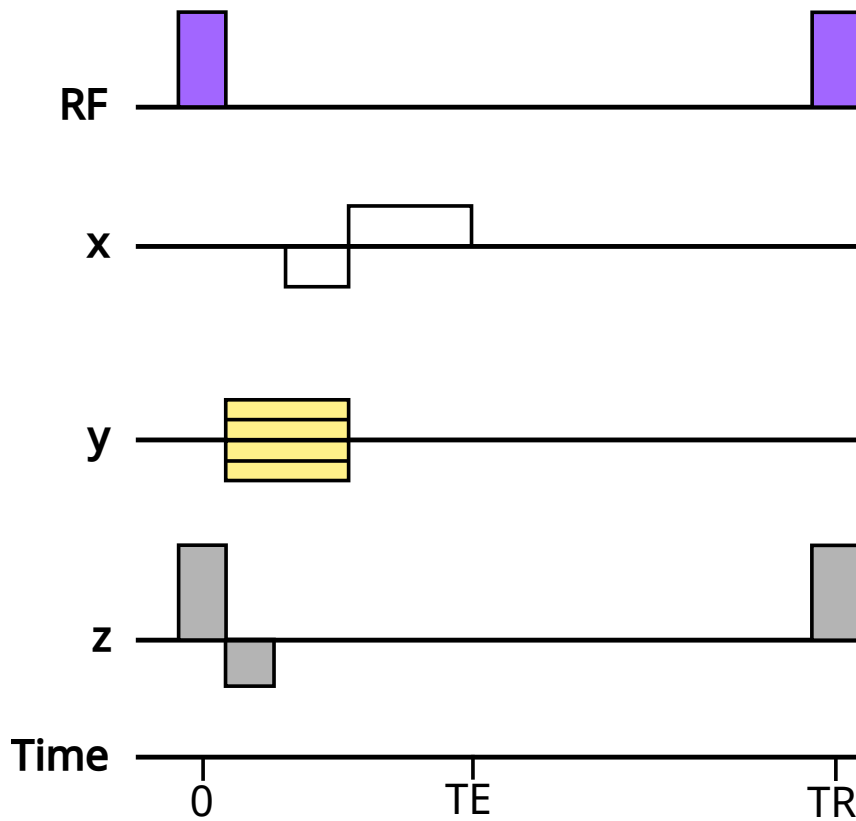
Figure 2.9: Basic gradient echo sequence where readout is along the x-gradient, phase selection is along the y-gradient and slice selection is along the z-gradient. Note that in reality, objects are not hard rectangles, as the gradient coils can not immediately switch from value to value. Instead, they look like trapezoids where the ramps indicate the gradual increase/decrease in strength.

frequencies in k-space are organized so the lower frequencies are near the centre of the grid. These frequencies provide the image with the base contrast. The higher frequencies reside outwards and this data relates to the details and edges of the image.

2.3.1 Frequency encoding

The frequency encoding is usually performed along the x-axis. The gradient that is applied is used to discern where the frequencies in the signal is originating from. Nuclei at the high end of the axis will experience a stronger magnetic field and precess faster than nuclei at the lower end, while nuclei at the isocenter experience no change as the gradient intersects origo. By applying the Larmor equation (2.4) to the effective field along x, the resonance frequency can be shown to be dependent on the position:

$$B(x) = B_0 + xG_x$$
$$\Rightarrow \tag{2.19}$$
$$f(x) = \gamma B(x) = \gamma B_0 + \gamma xG_x = f_0 + f_g(x),$$

where f_0 is the initial Larmor frequency and $f_g(x)$ is the linearly varying frequency offset. The signal intensities of these frequency offsets are used to determine the signal in each voxel.
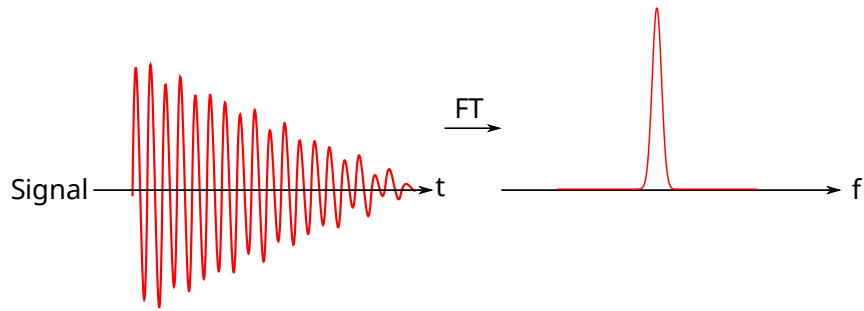
Figure 2.10: The Fourier transform of the signal gives a distribution of the precessional frequencies.

2.3.2 Phase encoding

Along the remaining axis, the signal is located with a phase-encoding gradient. After the phase-encoding gradient is turned off, the nuclei return to their initial precession frequency but along the axis, they have accumulated a phase shift according to the gradient. Since the strength, or slope, of the phase-encoding gradient changes every repetition, each individual gradient results in a linear phase in one direction over the object. This corresponds to one spatial frequency in k-space along that dimension. Different slopes of the linear phases correspond to different spatial frequencies.
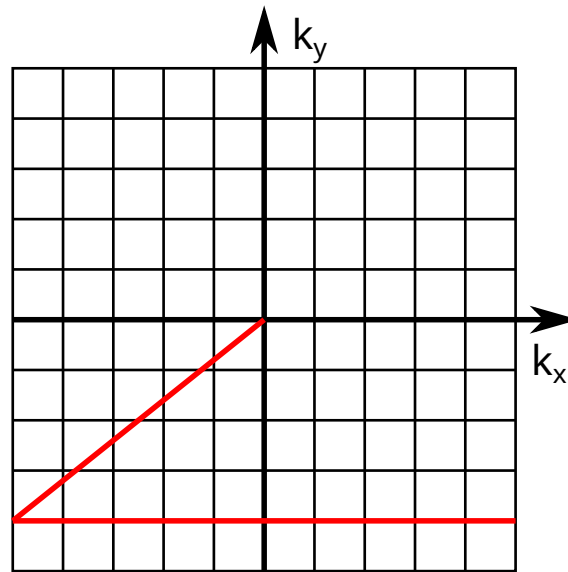
Figure 2.11: By varying the strength of the gradients one can traverse k-space and image it line by line.

Figure 2.11 visualizes how k-space looks along both encoding directions, denoted k_y and k_x, and how it is traversed. The starting point in the encoding process is in the middle of k-space before any gradients are switched on. The application of the phase gradient corresponds to moving along k_y and correspondingly the frequency gradient along k_x. The strength and polarity of the phase gradient determine which line is chosen and the dephasing gradient navigates the point to the leftmost side of k-space. The rephasing gradient is then applied and goes along the whole line at the same time as the signal is acquired. Varying the phase-encoding gradient each repetition allows the acquisition of the next lines. Because of the applied gradients, each data point contains phase and

frequency information from the whole slice and thanks to the Fourier transform of the waveform, each data point also contains information on the amplitude. When each line in k-space is sampled, the inverse Fourier transform of the whole matrix is applied and an image is produced.

2.4 B_0 inhomogeneity

2.4.1 Sources of inhomogeneity

MRI is a very sensitive form of imaging, and small irregularities can have a great impact on the image quality[2]. One of the most important factors is the homogeneity of the external B_0 field. The inhomogeneities in the field originate from a few different sources[8]. At delivery, the magnet itself does not produce a perfectly homogenous field due to imperfections in the magnet system. The effectiveness of the coils is especially sensitive to variations in the architecture and placements of the wirings. The surroundings of the MR site can also impact the homogeneity of the field. Depending on an object's size, magnetic permeability and distance from the magnet it can greatly distort the field. E.g. when planning a new MR site one would preferably avoid building close to elevator shafts and car parking lots. However, as these sources are static and can be limited, they are corrected on-site once the system is installed.

The most intricate form of inhomogeneity is however due to variations in the magnetic susceptibility of the imaging subject[9]. Magnetic susceptibility is an intrinsic property of a material, or tissue, which expresses its ability to become magnetized when exposed to an external magnetic field. Equation 2.20[10] describes the amount of magnetization for a magnetic field strength, H, due to the magnetic susceptibility, χ,

$$M = \chi \cdot H. \tag{2.20}$$

Substances with negative χ values induce a magnetic field opposite to the external field and are called *diamagnetic*. Correspondingly, substances with positive χ values induce a parallel magnetic field and are either *paramagnetic* or *ferromagnetic*. The effect of this additional magnetization is exaggerated at interfaces between tissues where the difference in susceptibility can lead to a sudden change in magnetization. Metal implants are big contributors to such differences as they are paramagnetic with quite large magnetic susceptibility. Interfaces are also found naturally in the body like the sinuses and the spinal cord, but are less profound. Note also that the shape and intensity of the magnetization are largely affected by the geometry of the interface and the magnitude of the susceptibility difference between materials or tissues.

When discussing the concept of relaxation it was mentioned that one of the factors of T2* dephasing is field inhomogeneity. The magnetization vector decays more quickly than expected by the intrinsic decay constant and a loss in signal is observed. In terms of the measured signal by the coil as seen in Figure 2.10, the measured frequencies will be more spread out. When the ROI is located in areas with high local field inhomogeneities, like those previously mentioned, it will make it difficult to examine and/or diagnose the subject.

Besides just a loss of signal and decrease in SNR, there is also another significant consequence of B_0 inhomogeneity. When performing the spatial encoding of a measurement,

the relation between spatial position and frequency is important. The gradients that are applied for spatial encoding will be disturbed depending on the inhomogeneities. For the frequency encoding this will lead to a frequency shift according to the change in magnetic field and the signal will be mapped to the wrong position. Figure 2.12 shows how the frequency ω is mapped to the wrong position because the gradient is altered. The consequence of Figure 2.12 can also be expanded to the slice selection gradient as the resulting slice that is excited will be observed at a different position than expected.
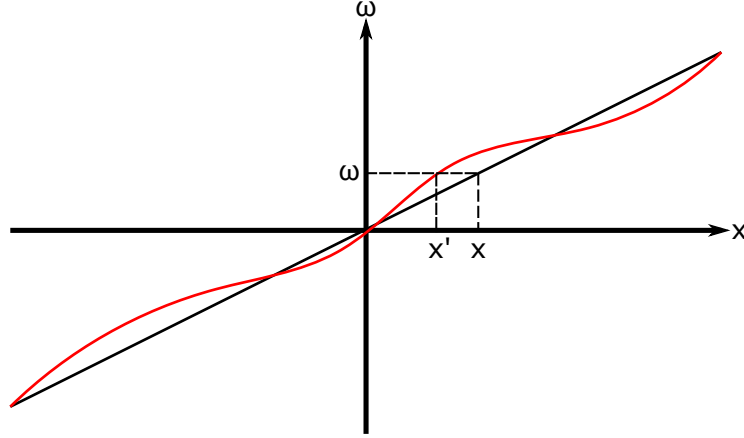

Figure 2.12: A gradient (black) in the frequency direction is affected by the inhomogeneity of the external field. This results in the observed gradient (red). The signal at position x' is now shifted to position x due to the inhomogeneity.

Another consequence of altered gradients stems from their new slope. The previous figure shows a discrete one-to-one of frequency and position, but in reality a bandwidth of frequency is utilized for both transmitting coils and receiving coils[1]. In areas where the slope becomes steeper than the original gradient, there will be less frequencies in the voxels and the signal is drawn out. If the slope is more gentle, there will be more frequencies within the voxels and the signal accumulates.

2.4.2 Field mapping

To visualize and identify the inhomogeneities of a magnetic field, a field map can be procured. A consequence of inhomogeneity is that the resonance frequency varies spatially. The longer the echo time of a measurement is, the more phase will accumulate. An expression for the phase after echo time TE and at a voxel in position $\bar{r}$ can be written as

$$\Psi(\bar{r}, TE) = \Psi_0(\bar{r}) + \omega(\bar{r}) \cdot TE, \tag{2.21}$$

where Ψ_0 is the initial phase and ω is the precessional frequency at the voxel[5, 11]. By taking two measurements with different echo times, the phase difference between them at each voxel is

$$\Delta\Psi(\bar{r}) = \Psi_2(\bar{r}, TE_2) - \Psi_1(\bar{r}, TE_1) = \Delta\omega(\bar{r}) \cdot \Delta TE_{1,2}. \tag{2.22}$$

By utilizing the Larmor equation (2.4), the phase difference can be used to express the magnetic field inhomogeneities as

$$\widehat{\Delta B} = \frac{\Psi(TE_2) - \Psi(TE_1)}{\gamma \Delta TE_{1,2}}. \tag{2.23}$$

Note that this equation is just an estimation as it does not include the stochastic noise found in every voxel. By including this in Equation 2.21 an expression for the measured phase is achieved.

$$\Psi_1(\bar{r}, TE_1) = \Psi_0(\bar{r}) + \omega(\bar{r}) \cdot TE_1 + \Omega_1(\bar{r}). \tag{2.24}$$

This can be utilized with the previous results to find the error of the estimate as

$$\varepsilon_{1,2} = \widehat{\Delta B} - \Delta B = \frac{\Delta \Omega_{1,2}}{\gamma \Delta TE_{1,2}}. \tag{2.25}$$

The take-away from this expression is that one can reduce the noise impact by increasing the echo time difference. However, increasing ΔTE too much will lead to a phase difference that causes wrap-around artifacts. This is because the phase offset has an observable range $[-\pi, \pi]$. Voxels falling out of this range will lead to abrupt changes in the field map called wrapping as the phase in the voxels wrap around to the other extreme of the range[12]. These wrap-arounds can also stem from strong local inhomogeneities which increase the rate at which the spins dephase. Figure 2.13 is an example of a field map from the preceding specialization project[5].
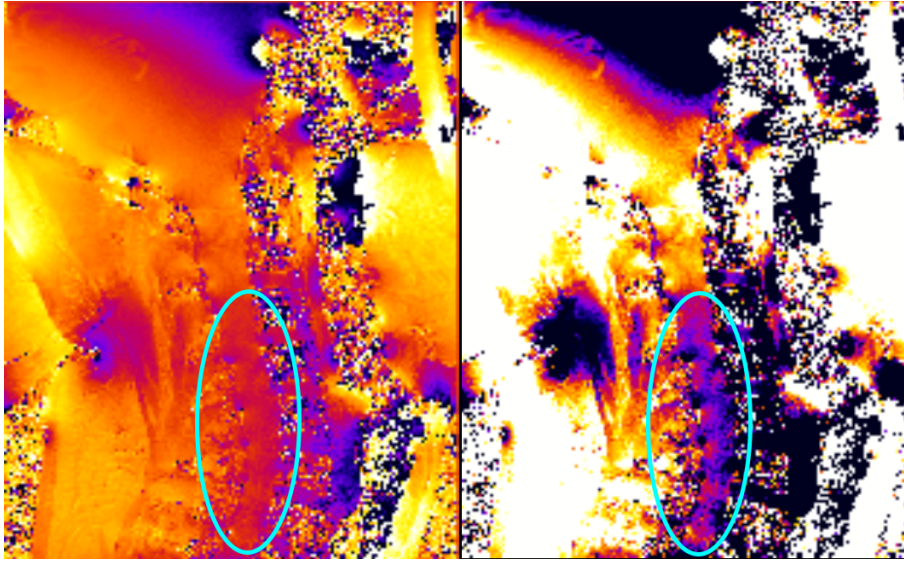

Figure 2.13: Field map from the preceding specialization project[5]. The highlighted area is the spinal cord which was the ROI of the project. The right image has its contrast adjusted to visualize the local field inhomogeneities between the intervertebral disks.

2.5 Shimming

2.5.1 Passive shimming

The process of compensating for B_0 inhomogeneities is called shimming. The most basic application of shimming is called *passive shimming* and is performed on every scanner at installation[1]. It involves fully or partially eliminating the sources due to the scanner itself and its surroundings at the MR site. Ferromagnetic plates can be strategically inserted into trays placed in the bore and act as countermeasures[9]. The homogeneity of the bore is investigated beforehand using a probe at different points which measures the flux density over a 40 cm diameter of a spherical volume (DSV)[1]. The resulting data can be used to calculate the optimal number and placement of plates. These shim magnet plates will however degrade over time due to the high temperatures in the bore from rapidly switching gradient current. Their magnetic permeability can be affected or the materials can become magnetized. Over time, the plates therefore need to be replaced and/or reorganized.

2.5.2 Active shimming

To compensate for magnetic susceptibility induced inhomogeneity, *active shimming* is performed on a patient-to-patient basis. The two types of coils used in active shimming are *superconducting* and *resistive* coils. Superconducting coils can be used as a supplement to passive shimming by applying a static shim. The superconducting coils are in some systems used in this way as they are well equipped for this task since they do not require additional current after they reach the superconducting state[1, 13]. Additionally, they are placed in the cryostat and are therefore less sensitive to the temperature changes than the shim plates. Resistive coils are placed closer to the bore and operate at room temperature[1]. Unlike the superconducting coils, they can quickly change current and are more suitable for rapid changes. The magnetic field in a source-free region follows Laplace's equation[14] and for the B_0 field in MRI it can be reduced to

$$\nabla^2 B_z = 0. \tag{2.26}$$

By using a combination of solid spherical harmonic functions, this equation can be solved in a spherical volume.

$$B_z(r, \theta, \phi) \approx \sum_{n=0}^{N} \sum_{m=-n}^{n} A_{n,m} r^n S_n^m(\theta, \phi). \tag{2.27}$$

The variables r, θ and ϕ are spherical coordinates which express the spatial dependency, while $A_{n,m}$ is the weighting of each function. $S_n^m(\theta, \phi)$ are functions of an all-real basis set consisting of linear combinations of the corresponding SH functions which again are a product of the Legendre polynomial $P_n^m(cos\theta)$ and $e^{im\phi}$. Table 2.1 shows the SH up to $n = 2$ in the Cartesian reference frame.

Each coil in the shim system functions as one of the spherical harmonics and the current applied determines its weighting. For the 1st-order shims, it is common to use the gradient coils as shim coils with a technique called gradient offset[1], where a small current is added

Shorthand	n	m	Function
Z	1	0	z
X	1	1	x
Y	1	-1	y
Z2	2	0	$z^2 - (x^2 + y^2)/2$
ZX	2	1	3zx
ZY	2	-1	3zy
X2-Y2	2	2	$3(x^2 - y^2)$
XY	2	-2	6xy

Table 2.1: List of spherical harmonics orders (up to n=2) and spatial functions together with the shorthand commonly encountered[13].

to represent the shim. For each order, more coils are needed to fulfil all the functions as it follows $2n + 1$. After the inhomogeneous field is identified, the different shim coils of the system are combined using different currents to correct the field.

2.5.3 Dynamic shimming

Since the solution to the Laplace equation is a sum of a number of spherical harmonic functions, one could think that if one had a large number of coils available to represent the functions, most inhomogeneous fields could be compensated for. However, the assumption of the Laplace equation is that it holds for a source-free region. The moment a subject is present in the bore, this falls apart and any number of coils would not necessarily be enough to perfectly create an opposite field. The aim of dynamic shimming is to decompose the harmonic problem into manageable problems. This could be done as *region-wise* shimming, where certain regions are imaged one at a time to provide the best shimming. Another method is the *slice-wise* method where the shim is specific for each individual slice that is imaged[13].

When defining an image volume, one decides parameters like the number of slices and the slice thickness. For a magnetic field that has inhomogeneities with a large polynomial degree, the slices can limit the problem close to first-order slopes. For every slice one image, the shim gradient then needs to match the slope of the inhomogeneity with opposite polarity. While the slice thickness is the defining factor in decomposing the problem in the z-direction, the in-plane resolution of the voxel replicates the method in the remaining dimensions.

The values used for every slice need to be calculated based on a field map of the subject. By using the trend from neighbouring slices/voxels, the shim values are determined. Additionally, the frequency offset from the gradient needs to be calculated and applied. Figure 2.14 illustrates that since the gradient must intersect with origo, a frequency offset likely occurs between the gradient and the inhomogeneous magnetic field. Appendix A goes into more detail about the calculations.
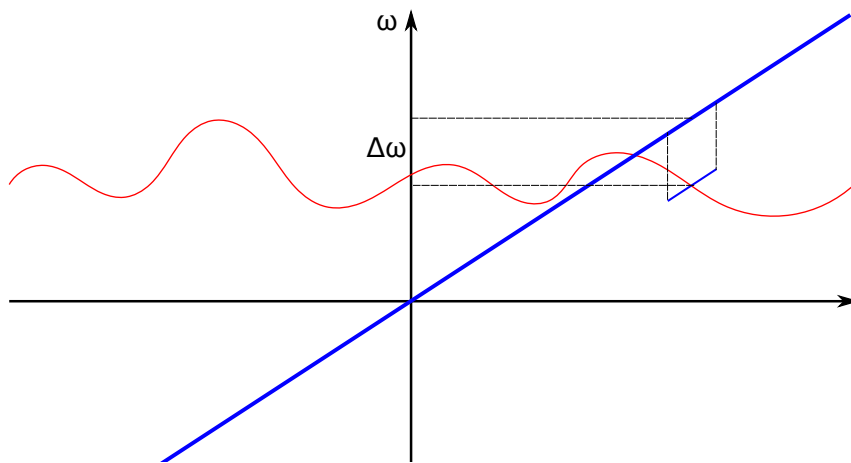
Figure 2.14: For each slice/voxel, a slope is drawn along the inhomogeneous field (red). The shim gradient (blue) is applied to compensate for the local field gradient, but will need a frequency offset $\Delta\omega$ to be correctly applied.

3 Methods

The following chapter describes the development of the code used with the dynamic slice-wise shimming method, the phantom validation tests and in-vivo experiments. The 7T Siemens Magnetom Terra scanner at St. Olavs hospital was used for all experiments with the 32RX/1TX head coil.

3.1 Development of slice-wise shimming method

There are several sequences provided by Siemens to be used on the scanner. The goal of the development was to implement the slice-wise shimming method on existing sequence code. All sequence code used in this project was in C++. Initial development and testing were done on a simple FLASH (Fast Low Angle Shot) sequence that only excited one slice. Mainly this was done to become familiarized with how the sequence code works, but also to start implementing the most basic features. The final method was developed on the gradient echo sequence. The basic setup of the sequence code was similar to FLASH, but the GRE code was more complex. The new features implemented in the FLASH code could therefore be with some modification duplicated to the GRE code.

To implement the gradient offset in the sequence code, one can either choose to send a command directly to the gradient amplifiers to change the offset current, or one can add additional gradient objects in the sequence. The former option requires the code to be interpreted and executed in real-time during the scan, and short waiting times need to be built into the sequence for this purpose. The latter option, of adding gradient objects to the sequence, was therefore considered to be less complicated and to interfere less with the sequence itself. Some experimenting showed that the gradient pulse objects could linearly stack with each other correctly and the choice of method was confirmed. The object simply had to be initialized and executed in the kernel that is run each TR. To shim for x, y and z simultaneously, one gradient object was created for each main gradient axis. For each TR, an object containing information about the current slice is available. The slice number was then pulled from this object and used to fetch the corresponding value from the vector.

For each slice, an offset to the demodulation frequency of the receiver objects also had to be added. This is because when the shims are applied, the nuclei are experiencing a slightly different magnetic field. This results in the object being shifted in the frequency direction according to the frequency difference as discussed in the theory section and shown in Figures 2.12 and 2.14.

As we want to provide the sequence with a list of shim values to apply, a function was needed to read a text file containing the values. This was done by creating a function that initializes a vector and places the values in said vector. The values in the vector were then applied to the gradient pulse objects on a slice-wise basis. The slice-wise shim values were calculated offline on a separate computer to the host. The resulting text file was organized as a matrix with four columns, the first three for each gradient object and the final for the
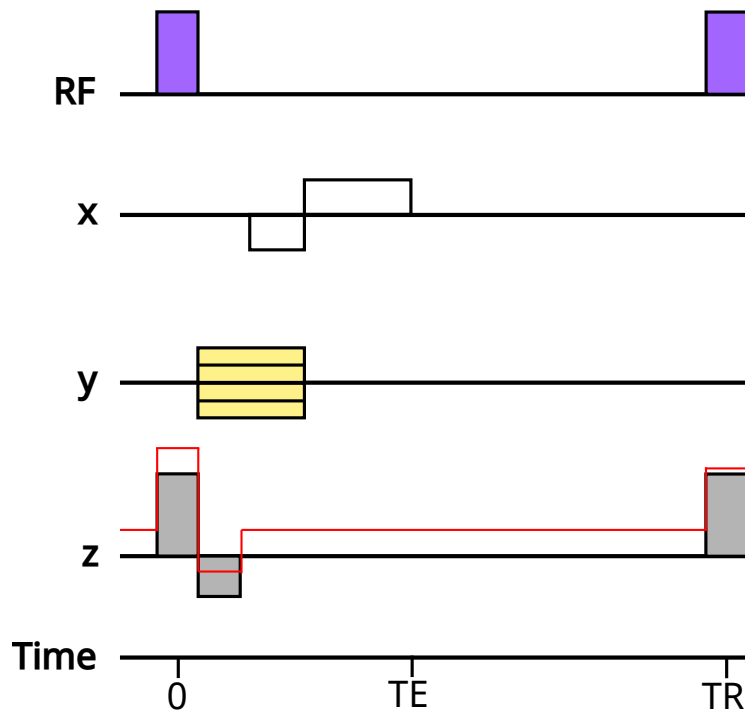
Figure 3.1: Objects in the sequence code stack so the shim gradient pulse object can be linearly added to the sequence. The figure shows how a shim (red line) in the z-direction would look in the basic GRE sequence. Every TR, the shim value can be changed.

frequency offsets with different slices along the rows. A test was implemented to ensure that there were enough values in the vector to cover all slices in the protocol. This meant that increasing the number of slices over the vector size would result in an error and abort the protocol.

Another problem to solve when dealing with gradient objects and multiple slices was the ramp up and ramp down time. A gradient coil can not simply be turned on and immediately reach the desired magnetic strength. The slew rate defines how fast the coil can increase its strength. The maximum slew rate for this system is 200 $mT/m/ms$, but a gentler slope of 180 $mT/m/ms$ was used to not risk exceeding the maximum. The system also has a certain limit to the total magnitude for each gradient direction, which is 3000 $\mu T/m$ in this case. This means that to turn on the gradient coil one would need 16.667 μs, or 20 μs to be safe, to reach the maximum limit. Additionally, the possibility of going from the minimum to the maximum (-3000 $\mu T/m$ to 3000 $\mu T/m$) between two slices needs to be taken into account. Thus the ramp up time has to be 40 μs. The ramp down time of one gradient object was set to overlap with the ramp up time of the next gradient object for the following slice. A test was also implemented to ensure that the total shim applied did not exceed 3000 $\mu T/m$ by checking the sum of the static shim and slice-wise shim for every slice.

3.2 Pipeline

The sequence code performing slice-wise shimming is only one part of the whole method. The first step is to find the actual values to apply and improve the image. The slice-wise
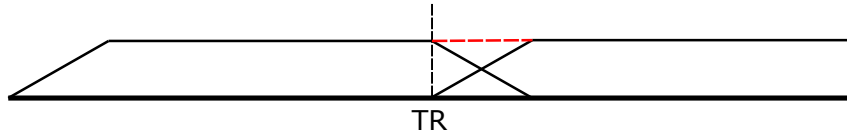
Figure 3.2: Illustration of two equivalent gradient objects and how the ramp down and ramp up cancel each other out. For all neighbouring gradient objects, the red, striped area becomes a linear combination of the respective ramps.

shim values were determined based on a high-resolution field map. The preceding project thesis used a MATLAB script to calculate and investigate shim values and frequency offsets with in-vivo data[5]. The same script was used in the pipeline for this project. The shim calculation is based on a linear fit of the measured field within a region defined by a mask. For the phantom, the mask was manually drawn and for the brain, it was defined using the software Brain Extraction Tool (BET) from the FMRIB Software Library[15, 16]. The script uses the measured field in the neighbouring slices/voxels to calculate the linear shim that is to be applied. Depending in the width of this inclusion, or slab width, a number of slices on the edges are therefore used in calculations, but not calculated themselves. The field map therefore needs to have a higher resolution in the slice direction and cover a larger field of view (FOV) than the image to be shimmed. A reference measurement with the same geometry as the image to be shimmed is needed to place the shim values at the correct positions. The resulting data from the first step is saved in a text file in the same format as used by the sequence code to read in the shim values. The final step is to make a measurement using the calculated shim values where the data is loaded by the sequence code and applied.

3.3 Phantom validation

To ensure the code was working as intended before moving on to in-vivo measurements, multiple experiments was run on a phantom. The code used in the first experiment was fairly basic and an additional goal of this experiment was to determine and visualize the remaining work needed for the final result. The two major features missing for this was the application of shimming in the x- and y-direction, and adding a frequency offset to the RF pulse corresponding to the shimming. These features were implemented after this experiment and used in the latter stages of the project. The remaining experiments were used to confirm the new features and work on the pipeline of the method for in-vivo measurements.

3.3.1 Basic sequence confirmation

For the very first experiment, several measurements were done using different lists of 20 shim values for the gradient in the z-direction. The purpose of this experiment was to confirm that the shim values from the list were applied to the intended slices. For this purpose, large z-shims were applied to selected slices of a GRE acquisition, to be able to see signal loss through dephasing in the shimmed slices. The images were acquired with the following parameters: $2 \times 2 \times 5$ mm^3 resolution, 20 slices, 250x250 mm^2 FOV, TR=500 ms and TE=20 ms.

Both an interleaved and ascending slice ordering was tested to ensure the shim values

were applied to the correct slice. In the case of the interleaved slice ordering, the scanner would image the odd-numbered slices first, before going back and imaging the remaining ten even-numbered slices. The ascending slice ordering is performed orderly one slice at a time. To reduce spin history and spoiler gradient effects which can affect the neighbouring slices, TR was increased to 2000 ms for this ordering.

The first measurement used a list which contained values alternating between 0 and 1000 $\mu T/m$. This should then give a result where every other slice is devoid of signal, while the rest are unaffected images.

The second measurement used a list which contained values ascending from 0 to 1000 $\mu T/m$ with increments of 50 $\mu T/m$. This should give a result where the slices are gradually losing signal.

3.3.2 Frequency offset application

In the second experiment, the frequency offset was tested. The alternating shim list measurement was repeated, but with a TR of 1000 ms and a distance factor of 100%. An odd number of slices, 11, was also chosen. Measurements were first taken without frequency offset. Then, using Equation 2.19, the frequencies of the shimmed slices were calculated by reducing the equation to the following

$$\Delta\omega = \gamma z G_z \tag{3.1}$$

The resulting frequencies were then applied to the sequence and a reference measurement was taken for comparison.

3.3.3 1st-order inhomogeneity tests

The third experiment was to test the pipeline of the method on 1st-order inhomogeneities. To simulate inhomogeneity in the phantom, a linear static shim was applied before measurements. The experiment was repeated for each direction with 100 $\mu T/m$ in the x-direction, -50 $\mu T/m$ in the y-direction and for the z-direction, measurements were done with both -1000 $\mu T/m$ and -150 $\mu T/m$.

The field map was acquired with 55 slices and 1 mm slice thickness using TR=2000 ms and two measurements with echo times TE_1=3.06 ms and TE_2=4.08 ms. Both magnitude and phase images were saved and transferred to an external computer for calculations. The field map was calculated and a mask was manually drawn for every slice of the phantom. A reference image of the phantom with 11 slices and 5 mm slice thickness was acquired beforehand and used to determine the shim values at the correct slice locations

The data was then loaded into the sequence and applied to compensate for the added static shim current. Additionally, reference measurements of the inhomogeneous phantom without compensation were acquired. All reference images, uncompensated and compensated images were also measured with TR=500ms and consecutively at 9 different echo times which are listed in Table 3.1.

Echo	TE (ms)
1	3.45
2	7.39
3	11.33
4	15.27
5	19.21
6	23.15
7	27.09
8	31.03
9	34.97

Table 3.1: Echo times for reference, uncompensated, and compensated measurements.

3.3.4 2nd-order inhomogeneity test

The pipeline was also tested on a 2nd-order inhomogeneity. For this experiment, the ZX-coil was used to simulate the inhomogeneity. The offset used on the coil was 500 $\mu T/m^2$. Otherwise, the method was performed with the same procedure and parameters as with 1st-order inhomogeneities.

3.4 In vivo measurements

A healthy volunteer was the subject of in vivo measurements to test the pipeline in brain imaging. The pipeline was looped two times. First with just the system tune-up applied which is the static shim applied to achieve homogeneity in a subject-free scanner. In this case the slice-wise shimming method does all the shimming specifically for the subject. Secondly with the global shim system applied which tries to compensate for the inhomogeneities in the ROI automatically. The slice-wise shimming was in this case used as a reinforcement to the standard active shimming.

The field map was acquired with the same parameters as previous pipeline tests, covering most of the brain in the imaging volume. Instead of manually drawing the mask of the brain, BET was used. The main images were acquired with the following parameters: $2{\times}2{\times}5$ mm^3 resolution, 20 slices, 250x250 mm^2 FOV, TR=854 ms and the echo times remained the same as in Table 3.1. As with previous pipeline experiments, images were acquired both with and without dynamic shimming applied.

In addition to dynamically shimmed images, an MP2RAGE sequence was used to achieve high anatomical quality images of the subject brain[17]. The sequence used 1 slab of 224 slices, TR=4300 ms, TE=1.99 ms and a resolution of $0.8{\times}0.8{\times}0.8$ mm^3.

4 Results

The following chapter presents the results obtained from the phantom validation experiments and the in-vivo measurements. All measurements were visualized using the NIfTI format image viewer MRIcron[18]. Additional figures and tables of interest can be found in Appendix B.

4.1 Phantom validation

4.1.1 Basic sequence confirmation

The first phantom experiment was used to validate an early version of the code. Figure 4.1 shows how the alternating list results in every other slice losing their signal due to the gradient offset being applied, while the remaining slices are as normal. Similar results were obtained using both interleaved and ascending slice order, confirming that each shim value is applied to the correct slice.

Results from measurements using the ascending list can be seen in Figure 4.2. The signal decreased rapidly with the increasing gradient offset and at 100 $\mu T/m$ (the third slice) the window settings had to be adjusted to properly visualize the slice. One can assume that values like this is where signal loss becomes more noticeable for measurements with these parameters. Figure 4.3 shows the fifth slice from this measurements with different window settings to highlight a region in the phantom, where local field inhomogeneity due to an air inclusion in the phantom caused signal loss in the unshimmed case, actually gained signal in the shimmed case.

4.1.2 Frequency offset application

Figure 4.4 displays three measurements; a reference, one where the shim is applied without the frequency offset, and one where the shim is applied with the manually calculated frequencies. The red lines in the figure shows that the frequency offset was successfully applied. Additionally, one can note that even for a small subject like a phantom, the positional shift is quite noticeable. The frequencies used and their positions are listed in Table 4.1.

Slice	Position (mm)	$\Delta\omega(Hz)$
1/11	±50	±2129
3/9	±30	±1277
5/7	±10	±426

Table 4.1: The manually calculated frequency offsets for the alternating list with offset 1000 $\mu T/m$.
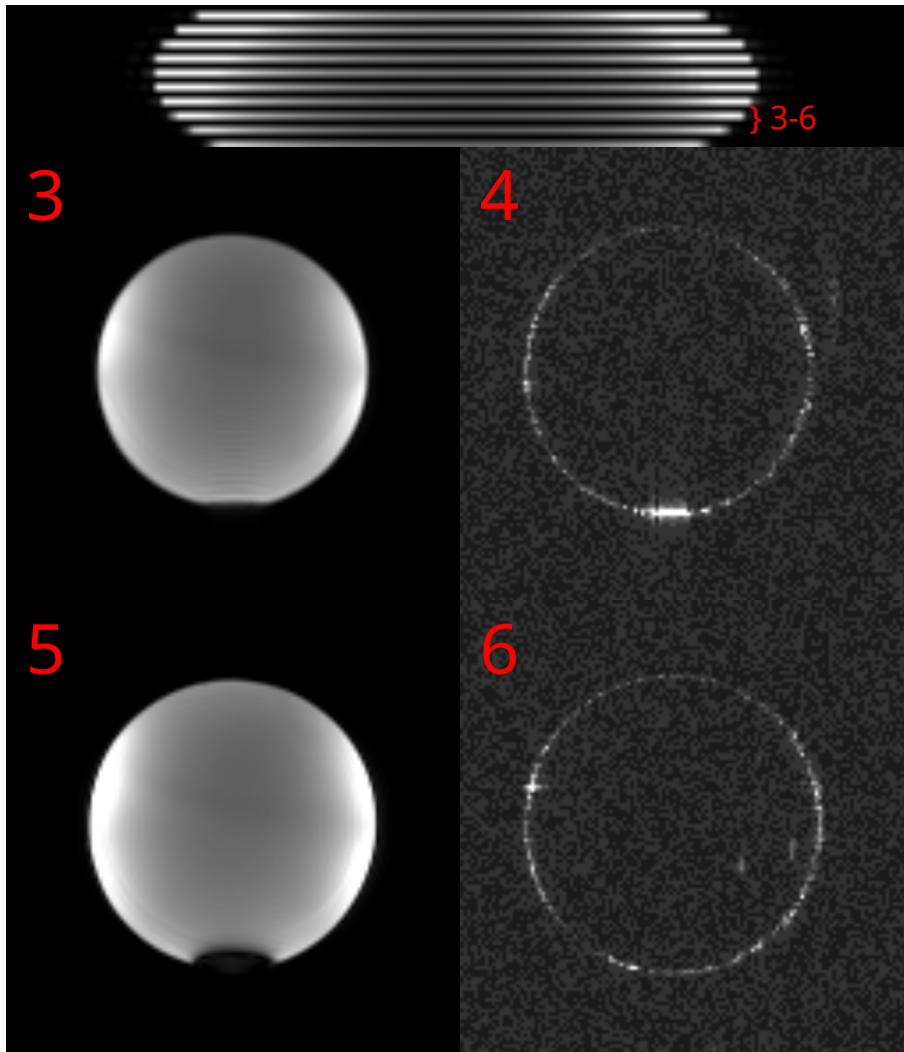
Figure 4.1: MRI scan of the phantom using the alternating shim list with an interleaved slice order. **Top:** coronal view of the phantom showcasing how every other slice has lost its signal due to the gradient offset. **Bottom:** four slices (3-6) of the phantom. To visualize the signal loss, the contrast of the shimmed slices were manually increased.

4.1.3 1st-order inhomogeneity tests

Field maps used for measurements in both 1st-order and 2nd-order inhomogeneity tests are displayed in Figure 4.5. This figure shows how the field maps follow the offset applied by the static shim coils. For the 1st-order tests, this is evident by the field maps following a gradient along the corresponding axis. For the 2nd-order test, this is visualized by a gradual change across both axes, especially noticeable by the darker spots in the lower-left and upper-right corners.

Measurements using a 1st-order Z-inhomogeneity were run twice: once with a larger, and once with a smaller shim offset. With a larger shim offset, wrapping occurred in the field map. This is visualized in Figure 4.6 which shows both a sagittal view of the field map and the calculated z-shim. The four valleys in the curve are a direct consequence of the black bands seen in the field map. Two of the slices corresponding to the image to be shimmed ended up in these valleys.
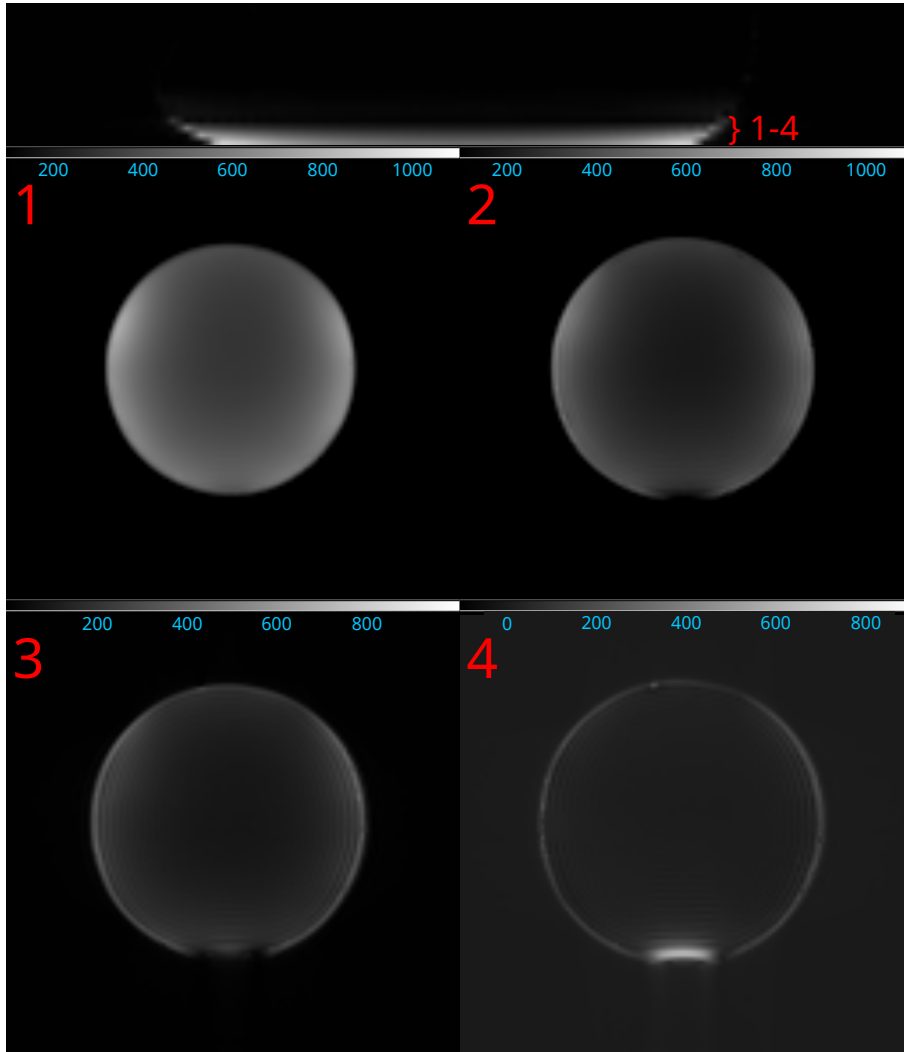
Figure 4.2: MRI scan of the phantom using the ascending shim list with an interleaved series. **Top:** coronal view showcasing how the signal quickly decreases due to the increasing gradient offset. **Bottom:** four slices (1-4) of the phantom. For visualization, the window settings were lowered while keeping the bandwidth consistent.

The measurements were repeated with the smaller offset and based on the calculations which are graphed in Figure 4.7 it is apparent that the shim is not perfect for the whole volume. However all shim values are within 50 $\mu T/m$ of the "true" value, 150 $\mu T/m$, with most being even closer which can be confirmed by consulting Table B.1. Figure 4.8 shows images from the fifth echo of the phantom measurement with and without the dynamic shimming method applied. With this figure, one can observe that the signal loss experienced at multiple slices is revived by the gradient offset. Note that for measurements like this with several echos, a late echo is chosen to allow the spins to dephase and make it easier to visualize the impact of the compensation in the figure. To further visualize the impact of the method, Figure 4.9 shows field map measurements of the phantom with and without compensation. In this figure, one can observe that the uncompensated field map follows the gradient along the z-axis. The compensation removes this trend and displays a homogeneous field map like the reference.

Images from the ninth echo of phantom measurements with X-inhomogeneity are found
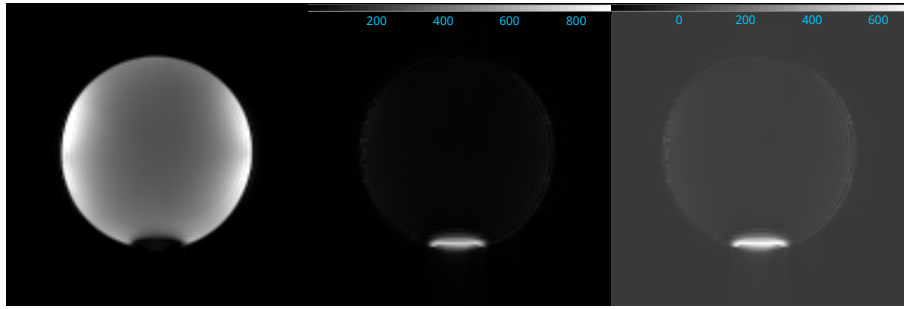
Figure 4.3: The fifth slice of the phantom from measurements with the ascending shim list showed a revival of signal in what was previously a signal void. For this slice, the shim value was 200 $\mu T/m$. **Left:** reference measurement with no shim applied. **Middle:** offset measurement with the same window settings as the standard. **Right:** offset measurement with adjusted window settings.

in Figure 4.10 which showcase in-plane distortion from B_0 inhomogeneity. Instead of great signal loss in the slice, one can observe a modest compression of the uncompensated phantom in the x-direction which the yellow lines are highlighting. Additionally, one can observe ripples in the image due to the inhomogeneity. Both the compression and ripples are however corrected with the slice-wise shim. Field map comparison is also included for this measurement in Figure 4.11. Similar to the Z-inhomogeneity, this shows how homogeneous the compensated field map is in comparison to the uncompensated.

Graphical and numerical results from the calculations of X- and Y-inhomogeneity can be found in Appendix B as Figures B.1 and B.2, and Tables B.2 and B.3. Additionally, equivalent image and field map comparisons for Y-inhomogeneity as with X-inhomogeneity are also included as Figures B.3 and B.4.

4.1.4 2nd-order inhomogeneity test

The calculated shim values for the ZX-inhomogeneity are graphed in Figure 4.12. Notice that the values are not symmetric around the isocentre, which is what one would expect from the ZX-inhomogeneity. The resulting measurement images at the ninth echo are found in Figure 4.13 where it is possible to see that the slice-wise shimming has improved somewhat on the signal. In the first slice, the compensated phantom looks improved on the right half, but at the same time has lost signal and become more distorted on the left in comparison to the reference. The sixth slice looks fairly similar uncompensated and compensated. From Table B.4 one can see that for this slice, S_z is close to zero while S_x is -18.3 $\mu T/m$. One can assume that in-plane distortion may have been compensated for correctly as the phantoms look equal in size, but the signal in the slice itself has not been improved since S_z is so low. The compensation for the eleventh slice looks similar to the first slice, although in this case, it is the left half of the phantom that has been well compensated and the right side which has experienced signal loss.

A field map comparison with and without compensation is shown in Figure 4.14. Overall the compensation looks to have been improved as the dark corners have been dampened. However, one can still observe a slight difference between the left and right of the field map along the x-axis. Note that the field maps are presented in a different colour scale to better showcase the inhomogeneous areas in the uncompensated phantom which spans from the upper-left to the lower-right corner in the coronal view.
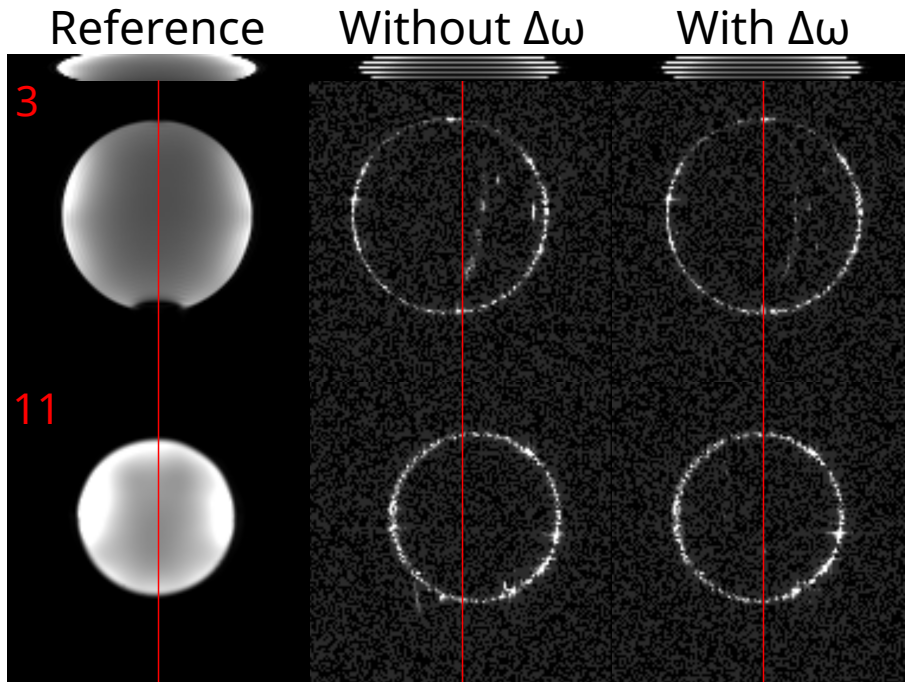
Figure 4.4: Three measurements of the phantom where slices 3 and 11 is representing the application of the frequency shift. A red line is drawn through the center of the images to highlight the positional shift. The coronal view of the measurement is included above each column. **Left:** reference measurement. **Middle:** measurement using the list alternating between 0 and 1000 $\mu T/m$, but without frequency offset applied. **Right:** measurement using the list alternating between 0 and 1000 $\mu T/m$ with frequency offset applied.
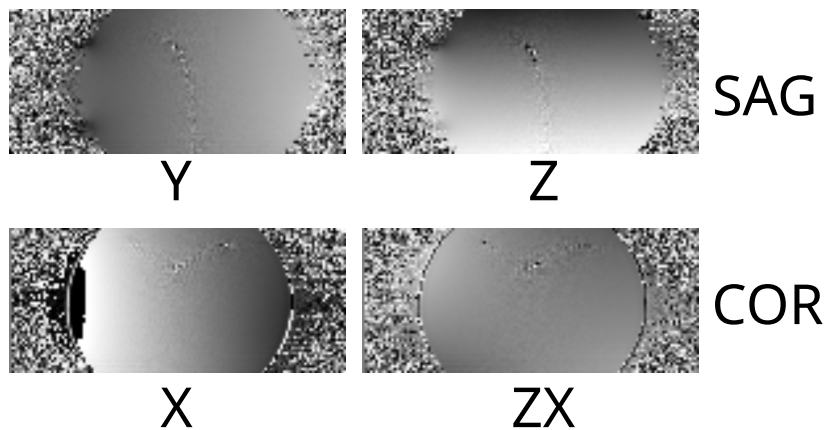

Figure 4.5: High-resolution field maps of the four measurements where a static shim is used to simulate 1st-order and 2nd-order inhomogeneities. Y and Z is shown in the sagittal plane, while X and ZX is shown in the coronal plane.
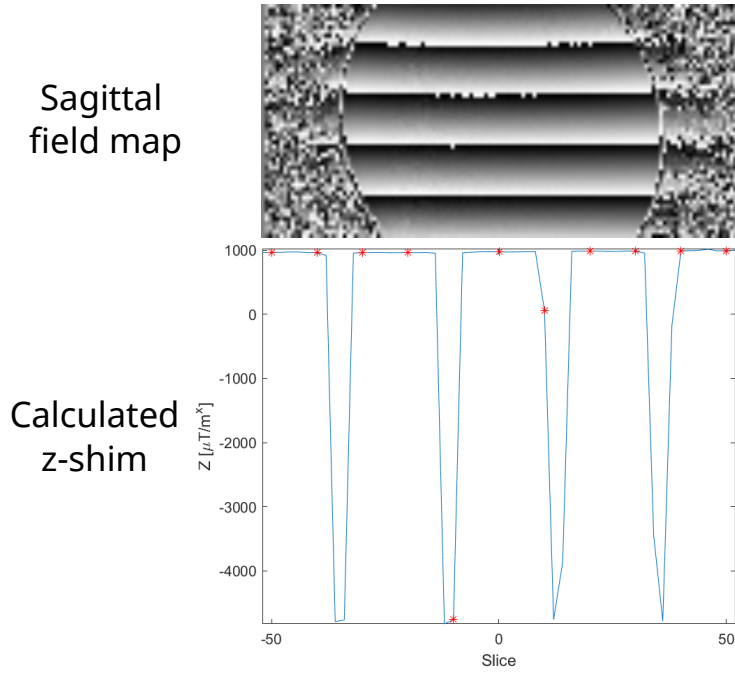
Figure 4.6: Field map and calculation results for the measurement with an inhomogeneous field in the z-direction of -1000 $\mu T/m$ where wrapping occurred. The red stars are the slice positions of the image to be compensated and two of these slices are positioned inside the black bands that create outlying shim values.

Figure 4.7: Calculation results from the 1st-order Z-inhomogeneity field map measurements with an offset of -150 $\mu T/m$. The graphs show the B_0 offset field and the shim values for the 1st-order shim coils. The red stars indicate the slice positions of the image to be compensated.

31

Figure 4.8: Slices 1, 6 and 11 of the measurement using a 1st-order Z-inhomogeneity of -150 $\mu T/m$ with and without shim compensation as well as a reference measurement. The images are from the signal at the fifth echo which had an echo time of 19.21 ms.
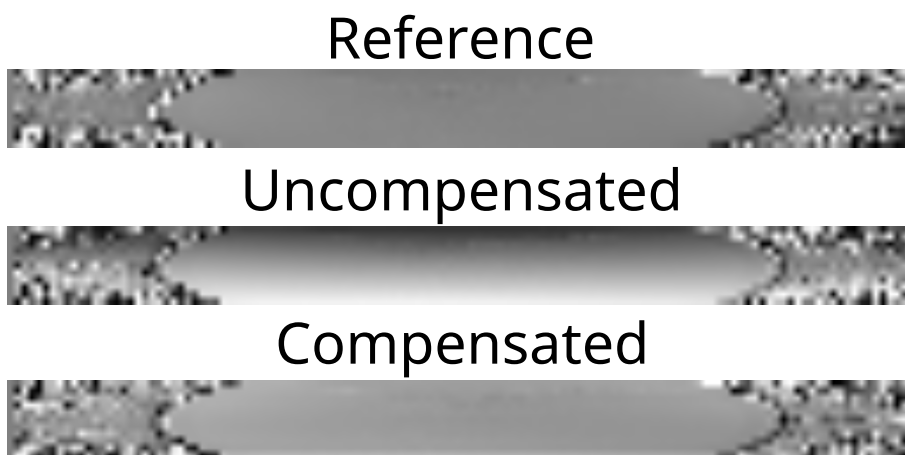
Figure 4.9: Field maps from 1st-order Z-inhomogeneitiy measurements. Shown in the coronal plane.
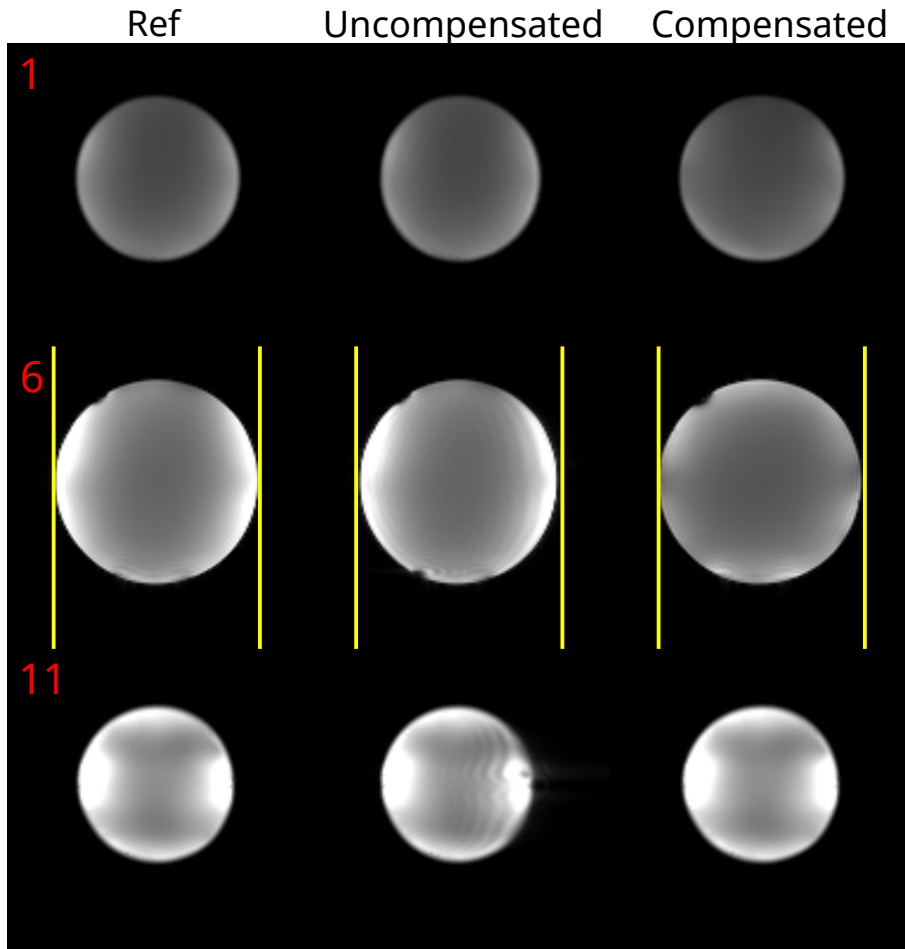
Figure 4.10: Slices 1, 6 and 11 of the measurement using a 1st-order X-inhomogeneity of 100 $\mu T/m$ with and without shim compensation as well as a reference measurement. The images is from the signal at the ninth echo which had an echo time of 34.97 ms. Notice how the phantom has been slightly compressed in slice 6 due to the inhomogeneity. The yellow lines are placed at the same position for each image to highlight this and how it has been corrected for with slice-wise shimming applied.
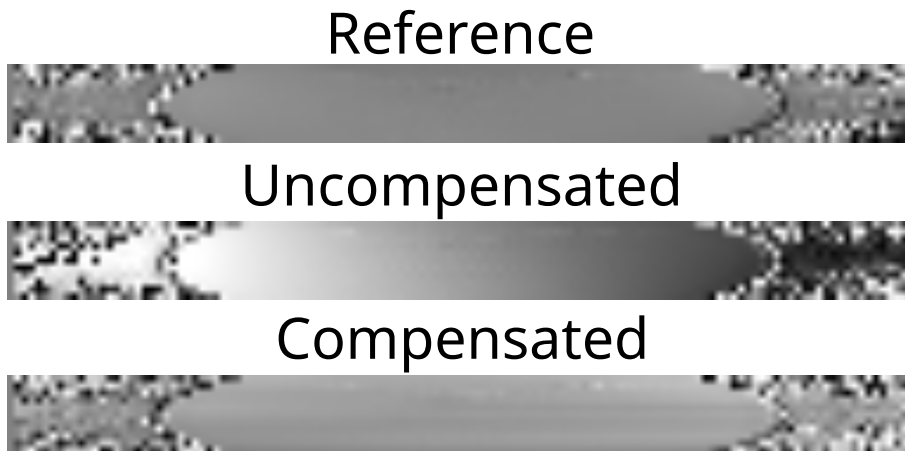
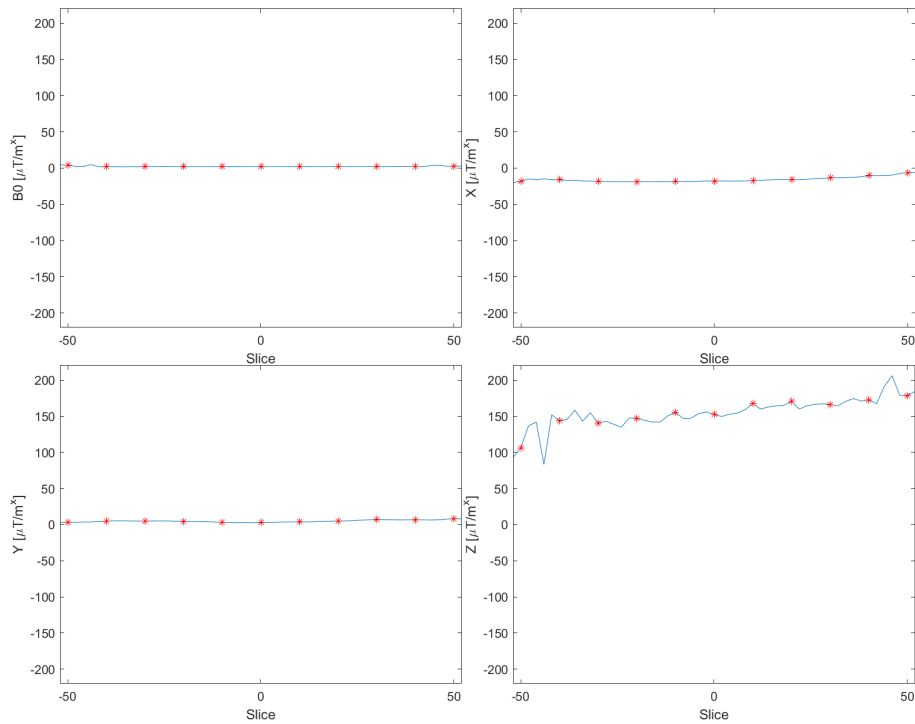Figure 4.11: Field maps from 1st-order X-inhomogeneitiy measurements. Shown in the coronal plane.
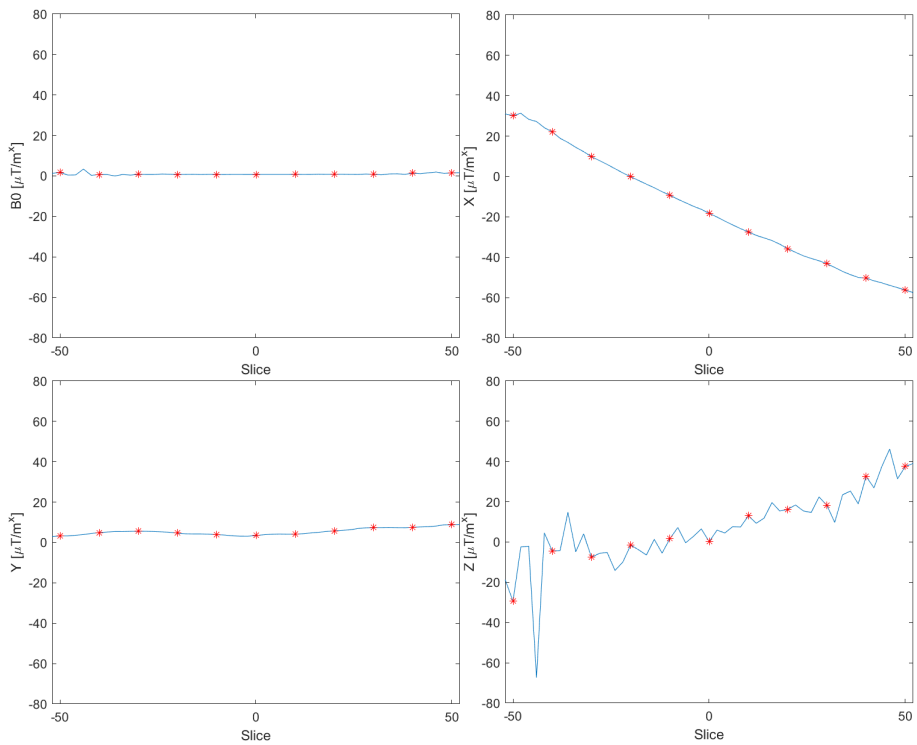
Figure 4.12: Calculation results from the 2nd-order ZX-inhomogeneity with an offset of $500\ \mu T/m^2$. The graphs show the B_0 offset field and the shim values for the 1st-order shim coils. The red stars indicate the slice positions of the image to be compensated.
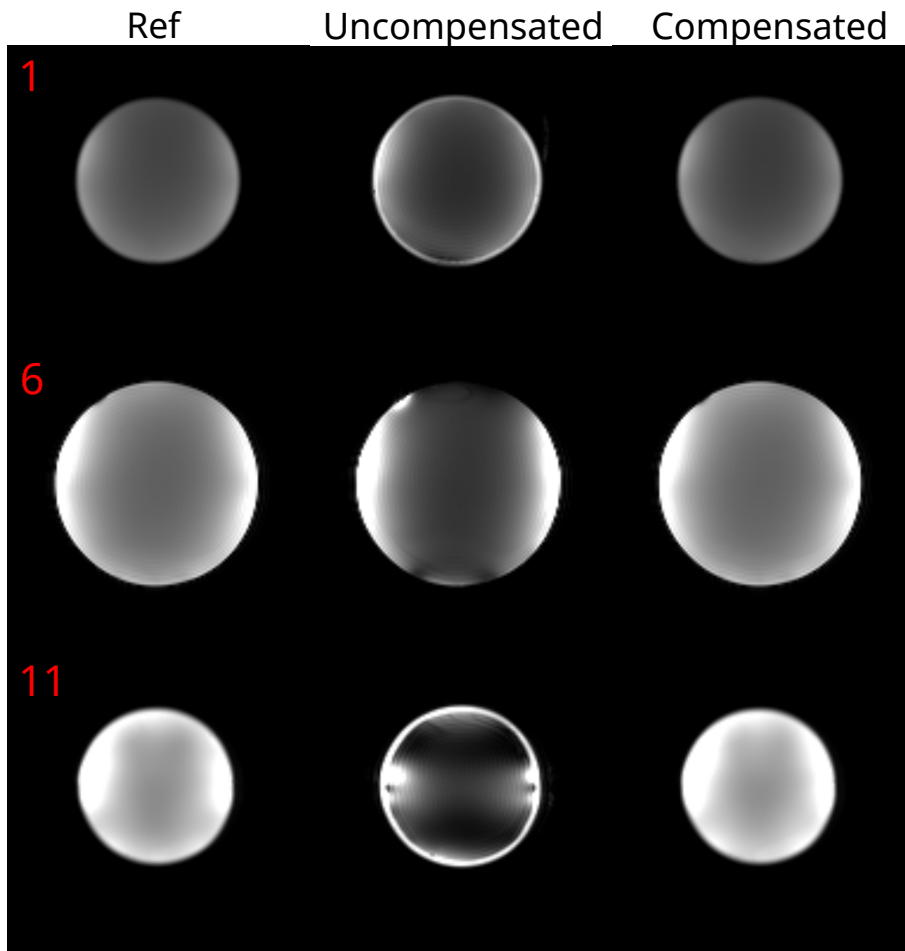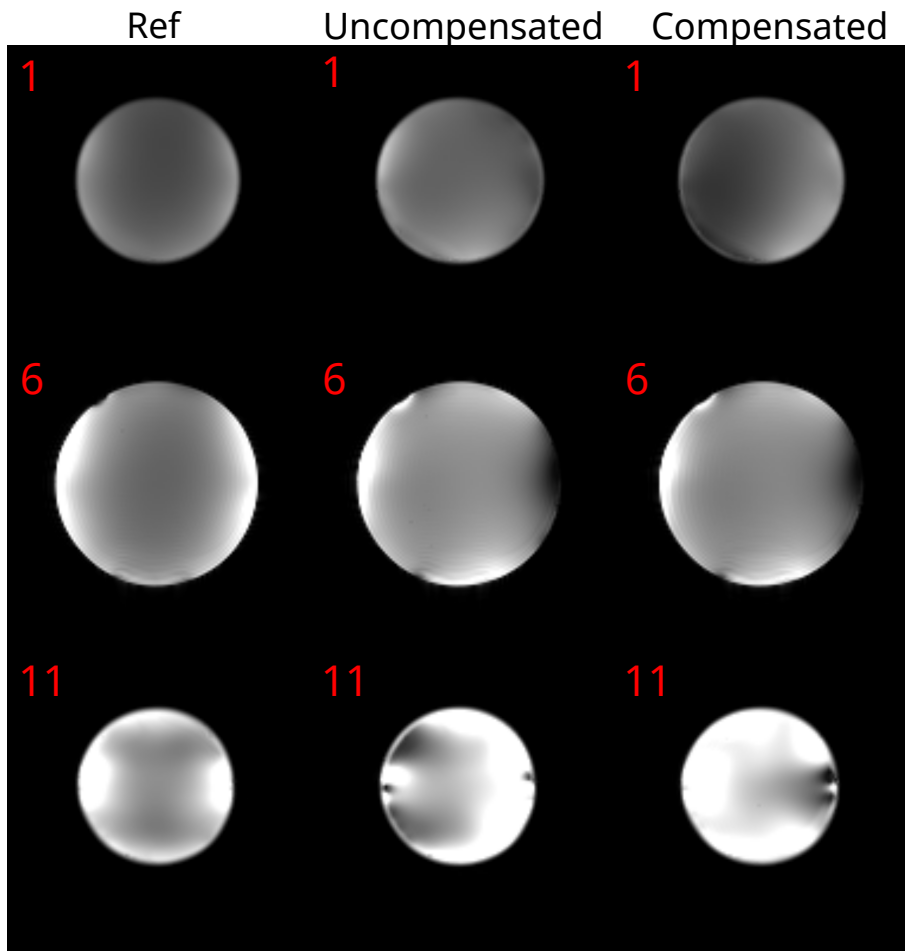
Figure 4.13: Slices 1, 6 and 11 of the measurement using a 2nd-order ZX-inhomogeneity with an offset of 500 $\mu T/m^2$. The figure compares the reference measurement with both uncompensated and compensated measurements. The images are from the signal at the ninth echo which had an echo time of 34.97 ms.
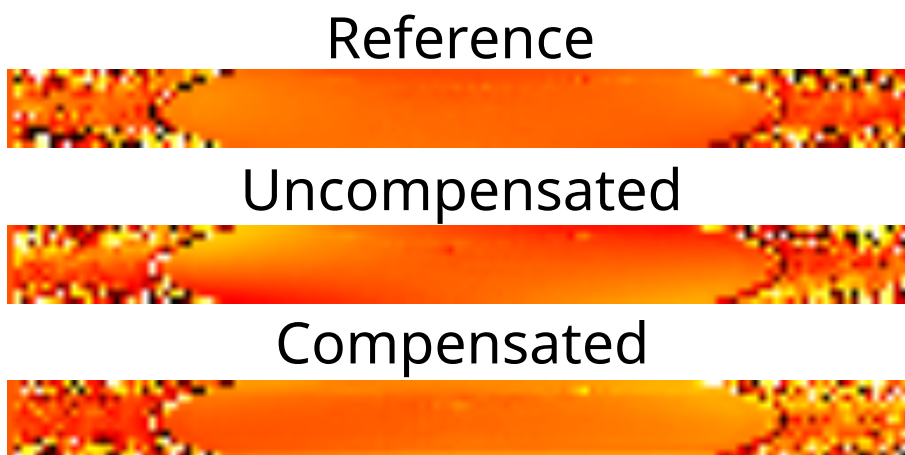
Figure 4.14: Field maps from 2nd-order ZX-inhomogeneitiy measurements. Shown in the coronal plane. The colour scale *1hot* has been used for easier visualization where black and white indicate $-\pi$ and π respectively and gradually change from red to yellow.

4.2 In vivo measurements

Figure 4.15 shows high anatomical quality images of the subject acquired with the MP2RAGE sequence. High-resolution field maps of the subject were acquired with tune-up only and with static shimming applied and are shown in Figure 4.16. The figure shows a lower slice where severe wrapping has occurred for the tune-up only measurement. The coronal and sagittal view also shows that this is not limited to one single slice, but is a feature of the lower part of the imaging region, around the front of the temporal lobe and the spinal cord. For the measurement with static shim applied, this wrapping is not present. However, Figure 4.17 shows that wrapping occurs around the sinus for this measurement which is not as severe for the tune-up only. While the static shim has improved the general homogeneity of the brain, it has aggravated it in this specific area.
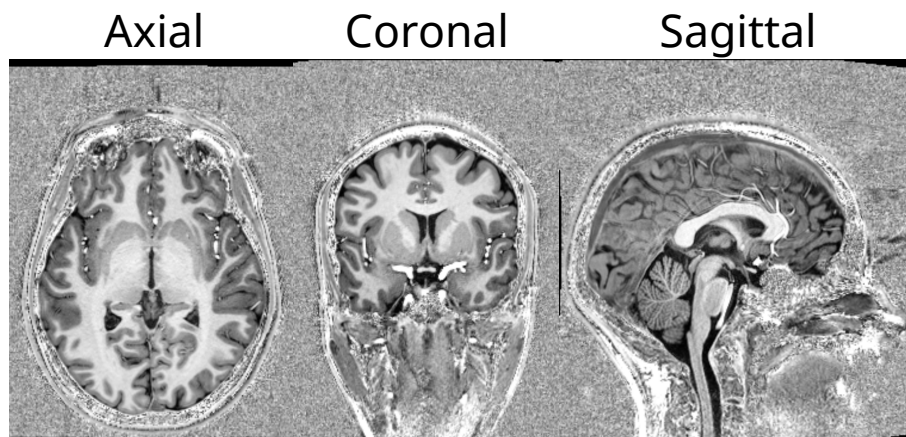
Figure 4.15: MP2RAGE images of the subject in the axial, coronal and sagittal plane.

4.2.1 Tune-up only

The resulting calculations of the tune-up-only field map resulted in some outlying values as expected, especially slices 1, 4 and 5 which can be found in Table B.5. The graphical results in Figure 4.18 also show that the wrapping has caused two valleys in the S_z-curve in this area. While local field inhomogeneities indeed can vary, one would not expect such drastic changes between slices and can assume these will produce a worse signal in the slice when applied.

As Figure 4.19 visualizes the impact of the application of these values a few observations can be made. Even though it is part of the lower region, slice 3 is exempt from the second valley in the S_z curve. The overall signal in the middle is improved which the difference of the images show. However, one can also notices that a lot of the details are missing from the slice-wise image and can be seen in the difference image where purple and black bands are visible in the upper and lower parts of the image indicating signal loss. To further investigate the measurements, field maps are included in Figure 4.20. Note that colors at either side of 0 from the color bar in the field map difference images does not inherently tell whether the signal has been improved or worsened. Dephasing can be relatively slower or faster and still result in a signal loss. For slice 3 a gradual shift in dephasing can be seen. Looking at the individual field maps, this is mostly due to the slice-wise shimming and matches the observation of signal improvement in the middle only.

Slice 5 has a major overall signal loss and this supports the assumption that the outlying

Figure 4.16: High-resolution field maps for both in vivo measurements. The blue crosshair is positioned at the same voxel for all imag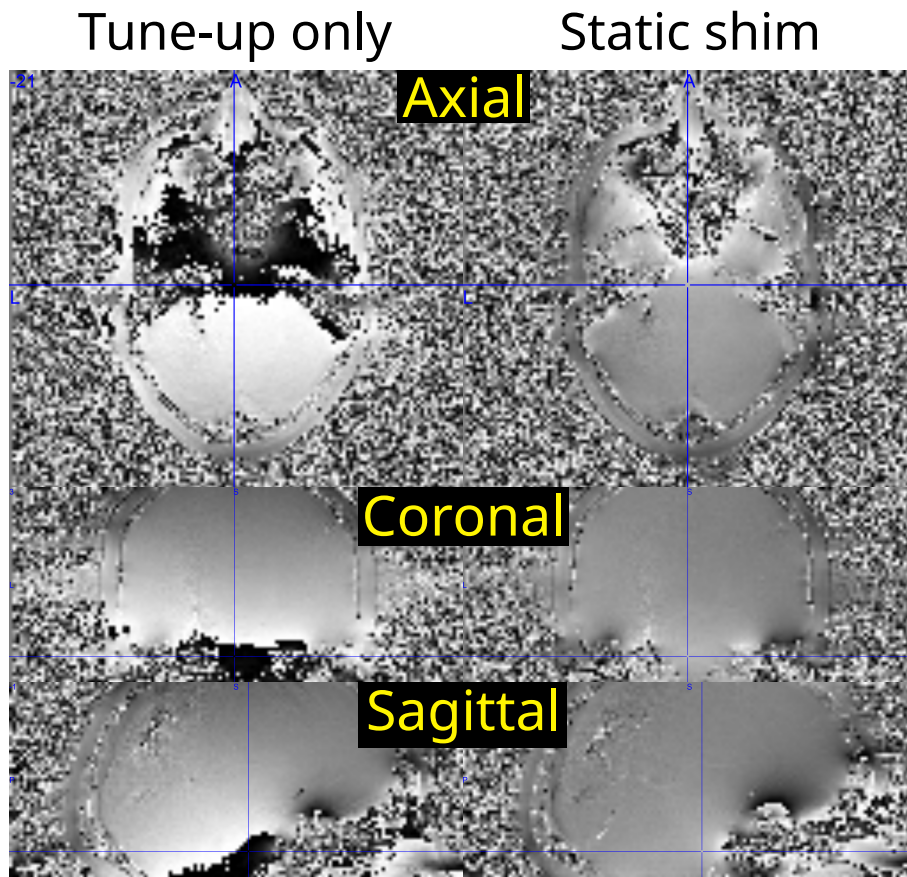es. The area presented is near the temporal lobe and spinal cord where severe wrapping occurred for measurements using tune-up only.
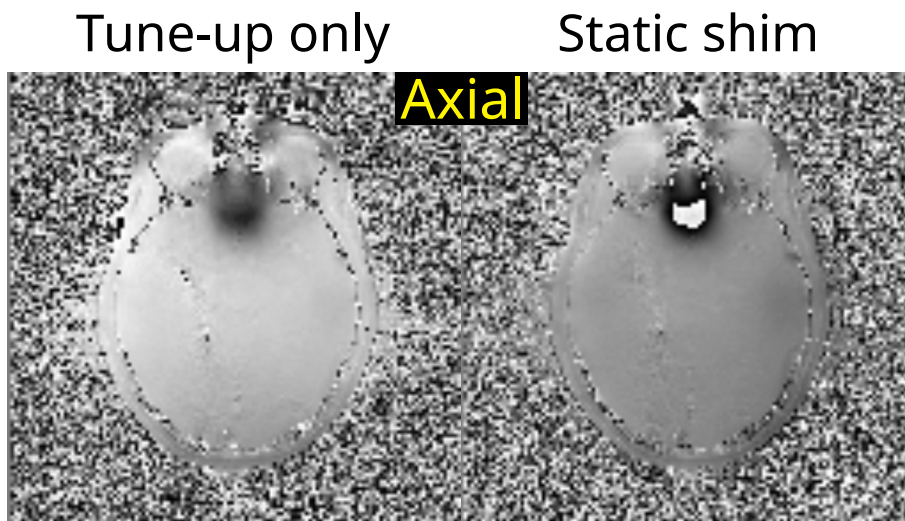
Figure 4.17: High-resolution field maps for both in vivo measurements. The slice in this figure is showing how the field maps behave around the sinuses.
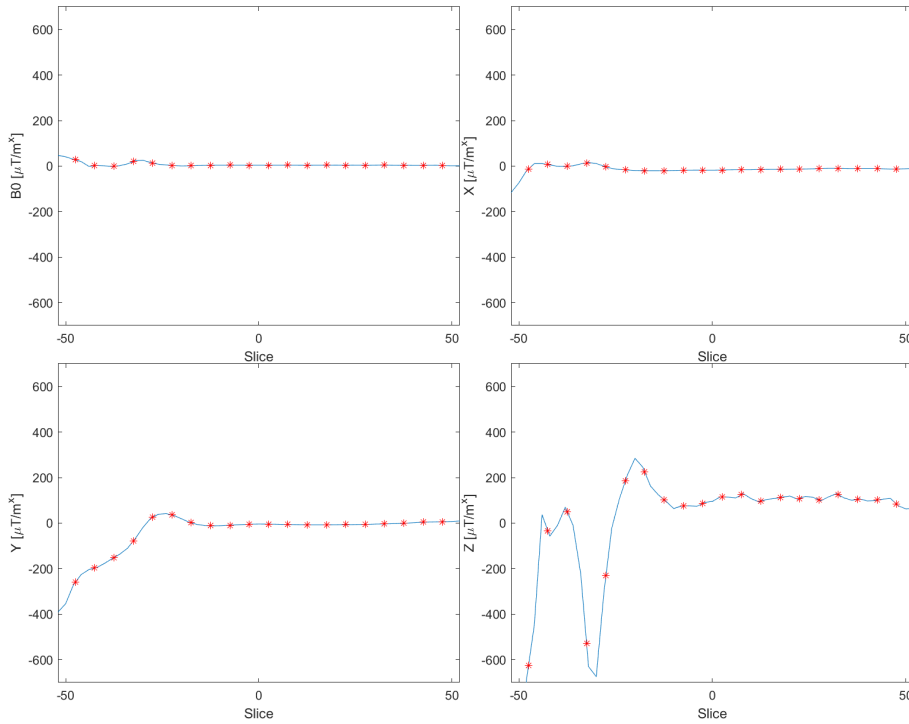
Figure 4.18: Calculation results from in vivo field map measurement with just the tune-up applied. The graphs show the B_0 offset field and the shim values for the 1st-order shim coils. The red stars indicate the slice positions of the image to be compensated.

values in the valleys are incorrect due to the wrapping in the field map. The field maps of the measurements for slice 5 also shows a significant difference as expected.

Further through the slices, number 7 shows a signal improvement in large areas in the front and middle, but loses signal in the back and around the auditory channels. Since the linear shims attempts to shim the whole slice at the same time, such trade-offs are given when the magnetic susceptibility in the slice varies. While the field maps shows a difference that could represent the signal improvement in the middle, it does not display anything connected to the auditory channels and back of the brain. One can however notice a spot in the front containing some irregularities.

In slice 11, the signal is improved over the whole slice except for one smaller area in the front. This is likely a consequence of the inhomogeneity from the sinuses. As with the previous slice, this becomes a trade-off where the overall slice is prioritized over a smaller area. The field map comparisons for this slice is nearly homogeneous and with a difference close to zero. As with the previous slice, one would expect some indication of the signal loss which for this slice is by the sinuses.

The last slice in the figure does not contain any major loss in signal and shows an improvement overall and especially on the sides. This is also displayed by the field maps which shows a homogeneous difference.

Figure 4.19: Slices 3, 5, 7, 11 and 17 of the measurements with tune-up only applied. The figure compares the field maps with and without slice-wise shimming applied, and the third row shows the uncompensated image subtracted from the compensated image. The blue marker on the colour bar indicates where 0 is. The images are from the signal at the fourth echo which had an echo time of 15.27 ms.

4.2.2 Static shim

For the second run of the pipeline in vivo, the slice-wise shimming was applied as a supplement to the standard static shim of the brain which would make the impact of the method more subtle.

Using Figures 4.22 and 4.23, similar comparisons can be done as for the tune-up measurement. Note that even though the color bar is the same, the changes for this measurements are more subtle which one notices by studying both nominal images before looking at the difference between them. Slice 3 from this measurement has a fairly similar result as previously as one can observe some improvement in the middle of the images, but several details and edges have their signal decreased. The field map comparisons tells an analogous story as for the tune-up measurement.

A large improvement between the measurements is seen in slice 5 as without wrapping it has been properly shimmed. Akin to slice 3 the signal has decreased somewhat in the edges, especially in the front and back of the brain. The field map comparison for this slice also supports this.

In slice 7 the side lobes of signal void is present both with and without slice-wise shimming. Similarly to the tune-up only measurements this has been aggravated while the middle part of the brain has seen some improvement. The field map comparison shows a gradual shift from left to right. From the image comparison this could relate to the signal loss being stronger on the left side of the brain.

Looking at the images from slice 11, the changes are quite subtle and the difference image shows both minor improvements and loss, mostly on the right side. This could explain the field map comparison which follows a gradient left to right.
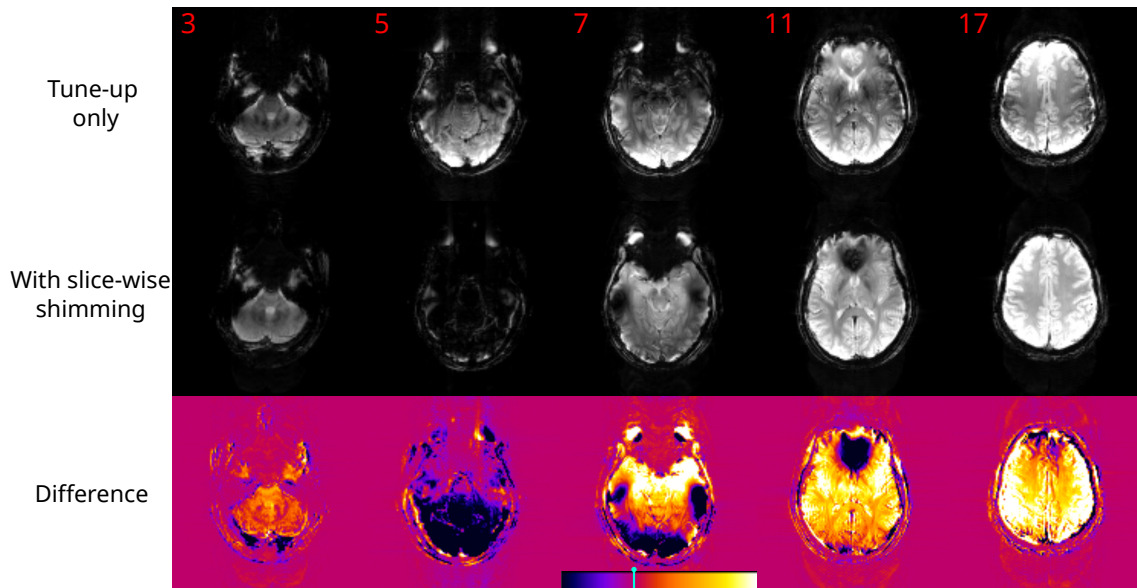
Figure 4.20: Slices 3, 5, 7, 11 and 17 of the field map measurements with tune-up only applied. The figure compares the field maps with and without slice-wise shimming applied, and the third row shows the uncompensated map subtracted from the compensated map. The blue marker on the colour bar indicates where 0 is. The images are from the signal at the fourth echo which had an echo time of 15.27 ms.

Slice-wise shimming for the last slice in the figures provides overall improvement with some signal loss in the edges. Compared to the other field maps from this measurement, the difference image is fairly homogeneous as well.
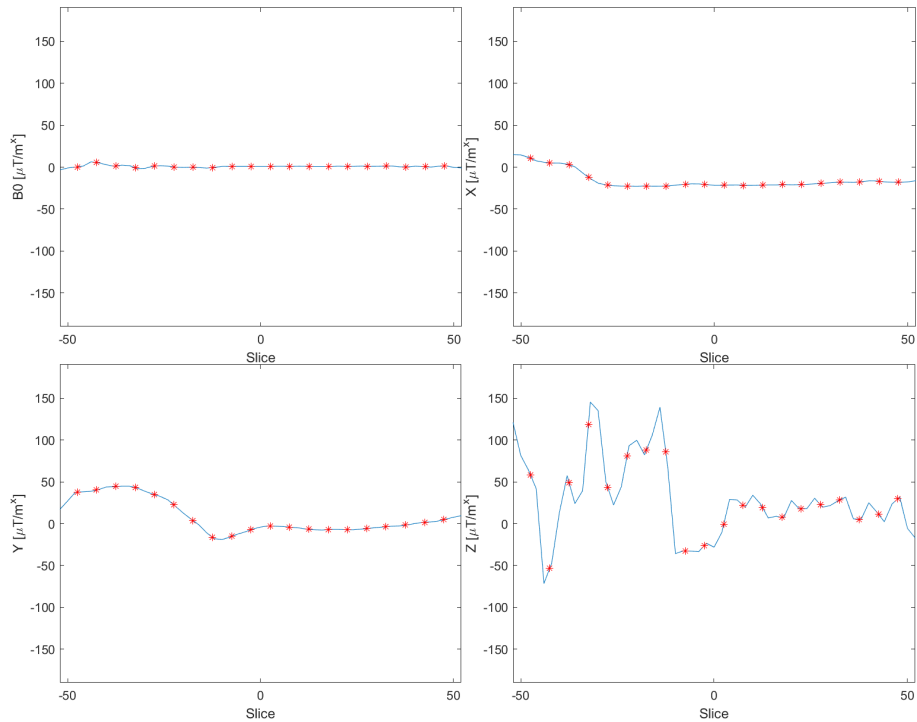
Figure 4.21: Calculation results from in vivo field map measurement with the static shim applied. The graphs show the B_0 offset field and the shim values for the 1st-order shim coils. The red stars indicate the slice positions of the image to be compensated.
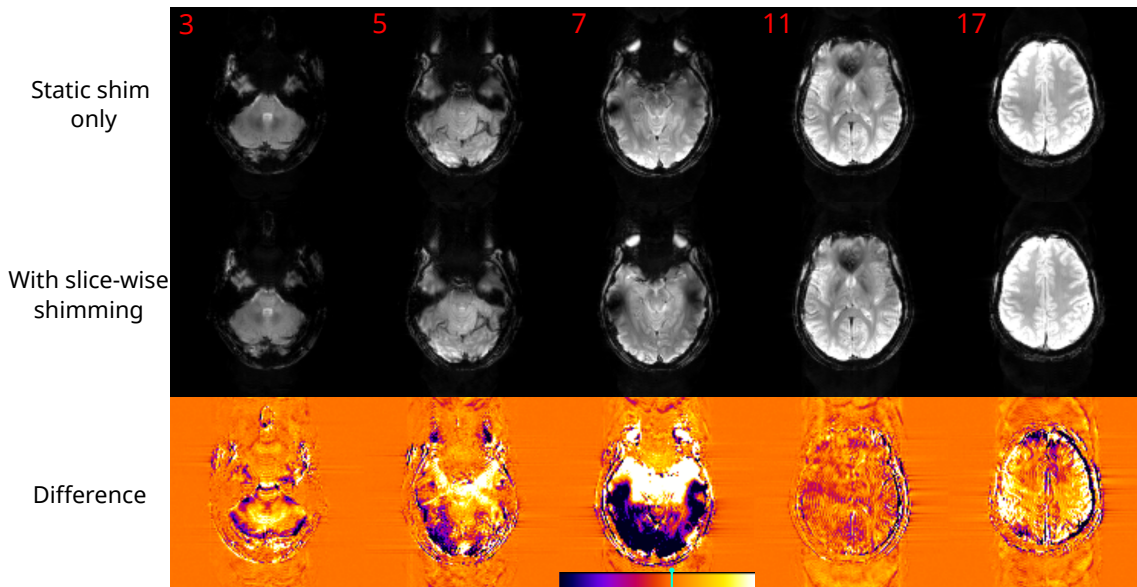
Figure 4.22: Slices 3, 5, 7, 11 and 17 of the field map measurements where the static shims are applied. The figure compares the measurements with and without slice-wise shimming applied and the third row shows the uncompensated image subtracted from the compensated image. The blue marker on the colour bar indicates where 0 is. The images are from the signal at the fourth echo which had an echo time of 15.27 ms.
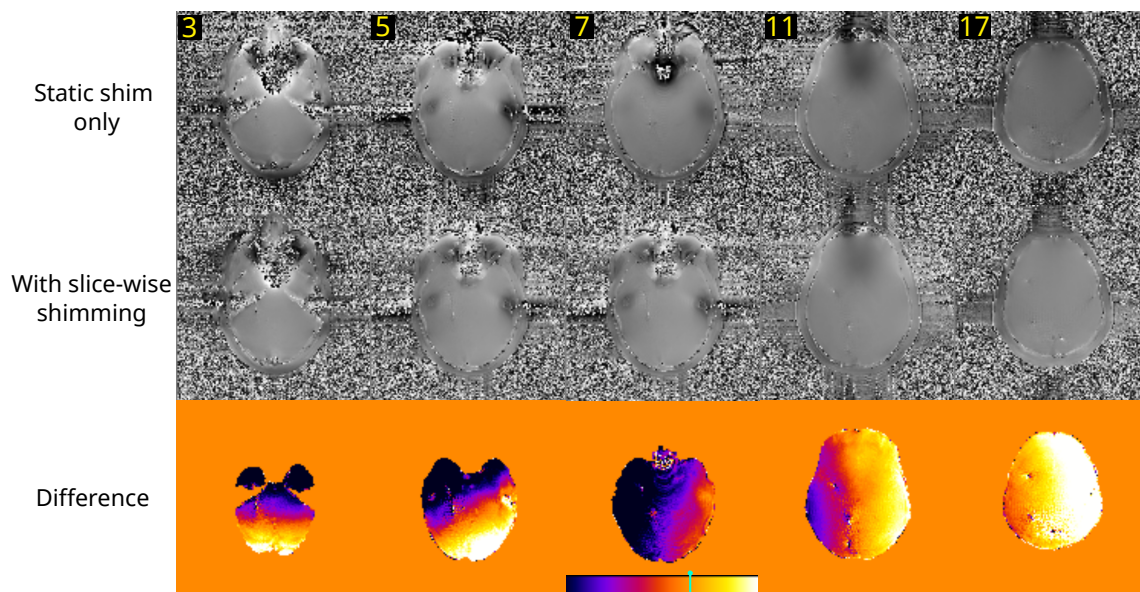
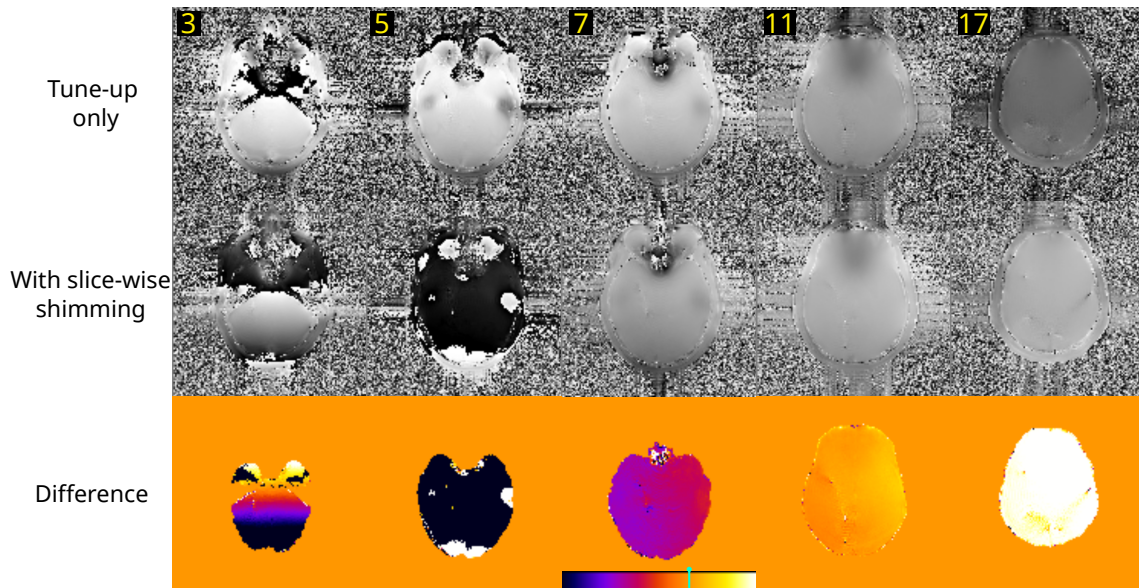Figure 4.23: Slices 3, 5, 7, 11 and 17 of the measurement where the static shims are applied. The figure compares the field maps with and without slice-wise shimming applied and the third row shows the uncompensated map subtracted from the compensated map. The blue marker on the colour bar indicates where 0 is. The images are from the signal at the fourth echo which had an echo time of 15.27 ms.

5 Discussion

5.1 Phantom validation

5.1.1 Geometrical application of shim values

The initial phantom measurements confirmed that the sequence code worked as intended regarding the application of shim values. However, during measurements with X- and Y-inhomogeneity, it was discovered that the x- and y-gradients were swapped between shim calculation and application in the sequence code. When calculating the shim values, they are assigned to the 1st-order coils, not the encoding direction. The kernel in the sequence code however does not discern between spatial directions, only encoding directions. In the sequence code, the y-shim was initialized in the frequency encoding direction. This is common for brain imaging where the long axis is anterior-posterior (AP) along the y-axis[1]. However this was not the case for the brain orientation used in this project and the X- and Y-coils were interchanged and applying the wrong value. This can change depending on the image orientation chosen at the measurement.

The pragmatic choice for this project was to simply switch the columns of the list so the values were applied to the correct coil. All measurements were made with the same orientation so the change had to only be made once. To improve the methods adaptability, the sequence code will have to accommodate the orientation as the calculations are strictly done in spatial coordinates. This can be done by fetching the image orientation and assigning the correct values to their corresponding gradient pulse object before the kernel is run. Figures 4.10, 4.11 and relevant figures from Appendix B showed that the switch worked and were applying the values correctly for the remaining coils as well.

5.1.2 Shim coil strength

The multiple phantom measurements also provided some intuition into the necessary magnitude of the gradient offsets for dynamic shimming. From the initial phantom tests, it was shown that offset values of 100-150 $\mu T/m$ were enough to both deteriorate the signal and also revive it in the phantom. This is dependent on image parameters like TE and slice thickness and may not be representative of in vivo imaging. By looking at Table B.5 which lists the shim values for the tune-up measurement one can see that the phantom values are actually quite comparable to S_z in many slices. The compensation needed for the static shim measurement was more delicate and consulting Table B.6 shows that most S_z values are well under 100 $\mu T/m$.

Additionally, with these kinds of values, one would expect to be safely within the total 3000 $\mu T/m$ gradient limit that was mentioned earlier. However, when wrapping of the field map occurs this can create cases where the calculated shim values are off by 5000 $\mu T/m$ like in Figure 4.6. To finish this particular measurement, the outliers were replaced with manually calculated values. To avoid this in further measurements, a reasonable

inhomogeneity was calculated to minimize the risk of wrapping. By finding the span of frequencies through the gradient over the phantom, this could be compared to the inverse of the echo time difference, $\frac{1}{\Delta TE}$. With $\Delta TE = 1.02$ ms, the inverse would be about 980.4 Hz. Bandwidths exceeding this number would result in wrapping, while bandwidths below should not. E.g. for the z-direction with 55 slices field map, 1 mm slice thickness and a distance factor of 100% would give a frequency span of

$$\gamma G_z(z_{55} - z_1) = \gamma G_z(54mm + 54mm). \tag{5.1}$$

For G_z=1000 $\mu T/m$ this results in a bandwidth of 4598.6 Hz and wrapping, while G_z=150 $\mu T/m$ gives 689.8 Hz and no wrapping.

5.1.3 Frequency shift

The positional shift from the frequency offset follows Equation 2.19 and as this effect scales with the position from the isocentre, the larger the imaging region is, the greater this effect can be if not compensated for. It should also be mentioned that the effect also scales with the intensity of the inhomogeneity itself. The receiving bandwidth of 800 Hz/px can be used in this case as it will predict how many pixels the subject is moved according to the frequency offset. With G_z= 1000 $\mu T/m$ the frequency shift at the furthermost slices from the isocentre would be half of the calculated bandwidth and the expected pixel shift would be

$$\frac{4598.6 Hz}{2 \cdot 800 Hz/px} = 2.87 px. \tag{5.2}$$

Note that the gradient applied is quite large, so the effect has been exaggerated for this measurement. However, for typical GRE measurements, the bandwidth is usually set as low as 200-300 Hz in the frequency direction. This means that even with a lower field inhomogeneity, the pixel shift can still be significant. This is even more consequential in the case of echo-planar imaging (EPI) where the bandwidth is as low as 20 Hz in the phase direction.

5.1.4 Effect of gradient offset

While the calculations of 1st-order inhomogeneities were consistent and provided adequate compensation, the effect of the 2nd-order compensation was not as clean. However, we know that we can never recreate a zx field with linear gradients, so we don't expect perfect compensation. The observation that the edge slices have a similar artifact, but are flipped, may imply that the combination of the coils are awry. Since the artifact is dependent on x it could be due to a misalignment of the S_x curve in Figure 4.12 which is not symmetric around the isocentre. Additionally, one can argue that since the curve of S_z is not as smooth as S_x, signal variation could be increased. This could also indicate that it was more difficult to determine the shim values in the z-direction. The combination of these factors could explain the difficulties with using 1st-order shims to compensate for higher-order fields.

5.2 Measurements in vivo

5.2.1 Tune-up wrapping

There are multiple ways to mitigate field map wrapping[11, 12, 19]. It can be done numerically by adding a phase-wrapping term to Equation 2.22 which forces the whole term to remain inside the interval $[-\pi, \pi]$ if it ever falls out. To minimize wrapping and noise accumulation concurrently, multiple measurements with different echo times can be taken and combined. Algorithms have also been developed that identify areas in the field map where wrapping has occurred and attempts to smooth it out and correct it. For this project, the FMRIB Software Library (FSL) was considered as it contains tools for unwrapping[16]. However, due to time restraints, this was not implemented in the pipeline in time.

5.2.2 Pipeline runtime

To make the MRI experience as comfortable as possible for the subject, the additional time when introducing special methods has to be considered. For this method, the pipeline has a couple of steps that increase the overall time the subject has to spend in the magnet bore. The first time-consuming part is the field map acquisition which requires two high-resolution measurements. Additionally, a reference image is needed to fit the shim values to the image one is shimming, bringing the number of additional measurements up to three. This is necessary for the calculation and there is no specific way to save time in this step other than to adjust the parameters of the acquisition for a lower duration if possible. Both the echo times and their difference was kept as low as possible for this project, and one would only increase the difference to reduce noise in the field map.

The step after field map acquisition is the one with the most potential to improve. Since the calculations were done on a separate computer from the host, the images were transferred over by USB stick. The field map calculations, automatic masking and determination of shim values in themselves are efficient. However, since the operations are done using different software, some time is spent switching and setting up each calculation. After calculations, the resulting text file then has to be transferred back to the host computer. By centralizing all these operations on the host computer one would not only save some time, but also a lot of hassle.

5.2.3 Signal improvement

For the in vivo measurements, the signal was generally improved for slices where the field map did not experience wrapping. The largest improvement is seen for the tune-up only measurement and shows that slice-wise shimming can work as a stand-alone method. The measurement with static shim has a more subtle signal gain.

An interesting response both measurements share is the local signal loss. Details, edges and specific areas experience diminishing signal while the rest of the slice improves. While the slices are thin in the z-direction and the shim value can be easily determined it is still an approximation of the whole slice. There are many voxels within the same slice and the z-shim will not be perfect for all voxels. Some areas will have local field inhomogeneities that are averaged out when the mask of the ROI covers the whole brain. The consequence

of this is that these areas may not be as well compensated or even experience a reduction in signal as seen in this project whether it be thin edges, the sinus or the auditory channels.

It would be interesting to further study the slice-wise method by investigating its impact on regions like those mentioned. Experiments could be done both with and without static shim applied to determine what is most beneficial for signal improvement in a specific area. The choice of mask would impact how local the shimming is and finding a good balance between increasing the signal in the ROI while not losing too much in the surroundings could be an additional objective.

5.3 Applications

A 2010 article by Juchem et.al. studied the effect of dynamic shim updating (DSU) on the human brain at 7T[2]. The study was inspired by previous research which showed how DSU of zero- to second-order shims at 4T improved homogeneity in the brain. Juchem's study took it a step further and included third-order shims to the method as a way to combat the increasing field inhomogeneities at ultra-high field MRI. The results showed an improvement compared to singular, static shim values. However, problems arose as eddy currents induced magnetic fields which degraded the homogeneity. The coils could be shielded to minimize this problem, but performing it for all 16 SH coils was not possible without losing some of the shimming effects. While the determination of slice-specific values was done effectively, the method required thorough calibration, characterization of the shim system and eddy current compensation which only increased with the order of shim coils. It was discussed how the relative gain of SH orders decreases with each inclusion. Second-order terms were shown to have the most substantial impact, and considerations must be taken into available equipment and resources to consider how many orders would be beneficial to include. The inclusion of second-order shims in this master's thesis could help reduce the local signal loss in the brain. However, one advantage this method has over multi-ordered DSU is the absence of eddy currents. Gradient coils are designed with eddy currents in mind and minimize their effect. This makes the method simpler and more practical to incorporate.

In 2011, Finsterbusch et.al. showed how slice-wise z-shim gradient pulses can improve fMRI in the spinal cord in 3T MRI[4]. Signal loss due to magnetic susceptibility differences between the vertebrae and the intervertebral disks can be detrimental in blood-oxygenation-level-dependent fMRI. Slice-wise shimming along the z-axis increased signal intensity and reduced signal variation. Additionally, by applying the z-shim *after* the phase-correction echoes, combined with flow rephasing in the same direction, ghosting artifacts caused by spinal-fluid flow were reduced. The article concludes that dynamic z-shimming could be beneficial in functional neuroimaging in the spinal cord. The spinal cord would be another interesting region to investigate with this master's thesis' method. Since this article only performed shimming in the z-direction and with a 3T scanner, it would be interesting to see if the method would still be beneficial for fMRI on UHF. While the z-shim is the most important aspect when considering the spinal cord inhomogeneity, comparisons could be made to see how much one would possibly gain from including the remaining shims.

Finsterbusch continued their work in a 2013 article which used DSU to shim the brain and spinal cord simultaneously[20]. In 2018, Islam et.al extended this work by shimming per-slice for both the brain and spinal cord on 3T[21]. Pathways and processes within

the central nervous system are complex and simultaneous imaging of the two regions can provide a greater understanding of its functions. As known, the spinal cord however has local field inhomogeneities that make this difficult. The dynamic per-slice method they developed improved homogeneity and they could perform fist-clenching fMRI experiments which produced consistent results between task activation in different parts of the brain. This is a good example of how the slice-wise method can be modified to improve signal in two different regions where the static shim could not properly compensate for the combination of the two. Further experiments with this master's thesis' method could try similar approaches on 7T MRI.

Dynamic slice-specific shimming has also been utilized in diffusion-weighted imaging (DWI) as Qui et. al. used it to improve rectal tumour imaging in 2021[22]. The study investigated both qualitative and quantitative performance compared with single-shot echo-planar imaging (SS-EPI) at 1.5T. Their method outperformed SS-EPI in both SNR, CNR, signal intensity and apparent diffusion coefficient (ADC) values. As surrounding tissue around the rectum like bones, bowel movement and bowel contents can produce B_0 inhomogeneity, their work may be greatly beneficial in improving image quality and lesion detection for rectal cancer. This shows how slice-wise shimming can be beneficial in other areas of the anatomy than just the brain. While the aim of this thesis has been in implementation and considering signal improvement, further study with emphasis on the detection and characterization of lesions in the brain would be greatly beneficial when considering the uses for slice-wise shimming.

5.4 Further work

While the slice-wise shimming method was implemented on a 7T scanner, there are multiple improvements and further work that can be done. The pipeline itself has three specific improvements to be regarded:

- **Make the sequence code adaptable to different image orientations:** To avoid future hassle and generalize the code, a small fix where the shim values are automatically assigned to the correct coil according to the image direction is necessary. The encoding directions should be available to fetch before assigning the values so this would be a fairly simple objective to achieve.

- **Incorporate unwrapping to the pipeline:** As seen in several measurements, wrapping can be detrimental to the determination of shim values. Incorporating an unwrapping technique would therefore be crucial in improving this method either by using the proposed software this project considered or a different approach.

- **Effectivize the pipeline:** As it stands the pipeline is quite sluggish as the steps were spread out over multiple computers. After field map measurements are acquired; calculations, masking and determining shim values have to be performed before the dynamic shim measurement can be performed. Centralizing and automatizing these processes would reduce the waiting time for the subject considerably.

A limitation of this project was also the number of in vivo measurements as there was only time to test the method on a single subject. Multiple brain measurements of both the same and different subjects could give more insight into the reproducibility and consistency of the method as is. Another thing to consider with the opportunity of additional measurements would be the choice of mask and ROI. The results from this project showed how a

trade-off occurred in some slices where the signal was improved overall at the expense of certain areas. Choosing smaller masks and ROI could be interesting to see the impact of the method on a specific area instead of the whole brain. From other studies, the spinal cord is a common factor regarding dynamic shimming and would be an appropriate choice to include in a future project with this method.

6 Conclusion

The main objective for this master thesis was to develop a slice-wise shimming method to correct artifacts and implement it on the 7T scanner at St. Olavs Hospital in Trondheim. By modifying the GRE sequence code from Siemens and combining it with previous work on slice-specific shim calculation, a pipeline was developed. A phantom was used to validate and in some cases improve or correct features of the method. After these measurements confirmed the method worked as intended, a healthy subject was asked to volunteer for in vivo measurements.

Results showed that slice-wise shimming improved overall signal intensity in the brain as a stand-alone application when only the tune-up of the system was in use. However, severe wrapping in the field map occurred in lower parts of the brain which created some irregular slices where the signal got worse. As a supplement to the standard static shim, the method made more subtle improvements in signal. The field map procured for this measurement did not result in any major wrapping, except for a smaller region around the sinuses. For both measurements, one could observe that the dynamic shimming method was limited by its low-order nature as some areas of the brain lost signal after compensation due to the gradient offset.

Even though the main objectives were met, improvements can still be made to the pipeline both by implementing an unwrapping step and making the whole process more efficient. Additional in vivo measurements would also be beneficial to further improve understanding of the applications and benefits of the method.

Bibliography

[1] C. Westbrook and J. Talbot. *MRI in Practice*. 5th ed. Newark: Wiley, 2018.

[2] Christoph Juchem et al. 'Dynamic shimming of the human brain at 7 T'. In: *Concepts in Magnetic Resonance Part B: Magnetic Resonance Engineering* 37B.3 (2010), pp. 116–128. DOI: https://doi.org/10.1002/cmr.b.20169.

[3] William T. Clarke et al. 'Multi-site harmonization of 7 tesla MRI neuroimaging protocols'. In: *NeuroImage* 206 (2020), p. 116335. ISSN: 1053-8119. DOI: https://doi.org/10.1016/j.neuroimage.2019.116335.

[4] J. Finsterbusch, F. Eippert and C. Büchel. 'Single, slice-specific z-shim gradient pulses improve T2*-weighted imaging of the spinal cord'. In: *NeuroImage* 59 (2012), pp. 2307–2315. DOI: https://doi.org/10.1016/j.neuroimage.2011.09.038.

[5] H. E. V. Skaldebø. *Implementing 1st-order slice-wise shimming for 7T MRI of the spinal cord*. Specialization project at Norwegian University of Science and Technology. Dec. 2021.

[6] V. Kuperman. *Magnetic Resonance Imaging: Physical Principles and Applications*. San Diego: Academic Press, 2000.

[7] N. Bloembergen, E. M. Purcell and R. V. Pound. 'Relaxation Effects in Nuclear Magnetic Resonance Absorption'. In: *Phys. Rev.* 73 (7 Apr. 1948), pp. 679–712. DOI: 10.1103/PhysRev.73.679.

[8] K. Wachowicz. 'Evaluation of active and passive shimming in magnetic resonance imaging'. In: *Research and Reports in Nuclear Medicine* 4 (2014), pp. 1–12. DOI: https://doi.org/10.2147/RRNM.S46526.

[9] C. Juchem and R. A. de Graaf. 'B0 magnetic field homogeneity and shimming for in vivo magnetic resonance spectroscopy'. In: *Analytical Biochemistry* 529 (2017), pp. 17–29. DOI: https://doi.org/10.1016/j.ab.2016.06.003.

[10] R. R. Freeman, J. A. King and G. P. Lafyatis. *Electromagnetic Radiation*. Oxford: Oxford University Press, 2019.

[11] F. Baselice, G. Ferraioli and A. Shabou. 'Field Map Reconstruction in Magnetic Resonance Imaging Using Bayesian Estimation'. In: *Sensors* 10.1 (2010), pp. 266–279. DOI: https://doi.org/10.3390/s100100266.

[12] J. Dagher, T. Reese and A. Bilgin. 'High-Resolution, Large Dynamic Range Field Map Estimation'. In: *Magnetic Resonance in Medicine* 71.1 (2014), pp. 105–117. DOI: https://doi.org/10.1002/mrm.24636.

[13] *Shim coil design, limitations and implications [Conference presentation abstract]*. International Society of Magnetic Resonance in Medicine. May 2006.

[14] K. Wachowicz. 'Evaluation of active and passive shimming in magnetic resonance imaging'. In: *Research and Reports in Nuclear Medicine* 4 (2014), pp. 1–12. DOI: https://doi.org/10.2147/RRNM.S46526.

[15] S. M. Smith. 'Fast robust automated brain extraction'. In: *Human Brain Mapping* 17 (Nov. 2002), pp. 143–155. DOI: https://doi.org/10.1002/hbm.10062.

[16] M. Jenkinson et al. 'FSL'. In: *NeuroImage* 62 (Aug. 2012), pp. 782–790. DOI: https://doi.org/10.1016/j.neuroimage.2011.09.015.

[17] José P. Marques et al. 'MP2RAGE, a self bias-field corrected sequence for improved segmentation and T1-mapping at high field'. In: *NeuroImage* 49.2 (2010), pp. 1271–1281. ISSN: 1053-8119. DOI: https://doi.org/10.1016/j.neuroimage.2009.10.002.

[18] Chris Rordens Neuropsychology Lab. *MRIcron.* Version 1.0.20190902. 2nd Nov. 2019. URL: https://www.nitrc.org/projects/mricron/.

[19] A. K. Funai et al. 'Regularized Field Map Estimation in MRI'. In: *IEEE Transactions on Medical Imaging* 27.10 (2008), pp. 1484–1494. DOI: 10.1109/TMI.2008.923956.

[20] J. Finsterbusch, C. Sprenger and C. Büchel. 'Combined T2*-weighted measurements of the human brain and cervical spinal cord with a dynamic shim update'. In: *NeuroImage* 79 (2013), pp. 153–161. DOI: 10.1016/j.neuroimage.2013.04.021.

[21] H. Islam et al. 'Dynamic per slice shimming for simultanious brain and spinal cord fMRI'. In: *Magnetic Resonance in Medicine* 81.2 (2019), pp. 825–838. DOI: https://doi.org/10.1002/mrm.27388.

[22] J. Qui et al. 'Integrated slice-specific dynamic shimming diffusion weighted imaging (DWI) for rectal Cancer detection and characterization'. In: *Cancer Imaging* 21 (2021). DOI: https://doi.org/10.1186/s40644-021-00403-9.

[23] S. Axler. *Linear Algebra Done Right.* 3rd ed. New York: Springer, 2015, pp. 111–112.

[24] D. A. Belsley, E. Kuh and R. E. Welsch. *Regression Diagnostics: Identifying Influential Data and Sources of Collinearity.* New York: John Wiley Sons, 1980, pp. 100–104.

A Slice-wise shim calculation

This appendix contains the theory section regarding slice-wise shim calculation from the specialization project "Implementation of 1st-order slice-wise shimming for 7TMRI of the spinal cord"[5].

To calculate the shim gradients for each slice, the following matrix equation on the form $b = Ax$ needs to be solved:

$$
\begin{bmatrix} \Delta\omega_1 \\ \Delta\omega_2 \\ \Delta\omega_3 \\ \vdots \\ \Delta\omega_N \end{bmatrix} = \begin{bmatrix} s_{x1} & s_{y1} & s_{z1} \\ s_{x2} & s_{y2} & s_{z2} \\ s_{x3} & s_{y3} & s_{z3} \\ \vdots & & \\ s_{xN} & s_{yN} & s_{zN} \end{bmatrix} \cdot \begin{bmatrix} a_x \\ a_y \\ a_z \end{bmatrix}
$$

Each slice yields a unique matrix equation with a number of voxels N. The left side of the equation contains a vector filled with phase offsets, $\Delta\omega_n$, for each voxel. On the right side, there is a matrix containing shim components in each voxel for the three shim channels x, y, and z. The shim components represent the gradient along the relevant direction in the voxel. Multiplied with the matrix is a vector containing the shim current a for each direction. The phase offset in a voxel is therefore defined as a linear combination of the shim components and their currents.

$$
\Delta\omega_n = s_{xn} \cdot a_x + s_{yn} \cdot a_y + s_{zn} \cdot a_z \tag{A.1}
$$

The field maps provide the phase offsets in each voxel for the left-side vector and are expressed in Hz. Since the right-side vector contains shim currents in ampere (A), the shim components in the matrix should be Hz/A. By calibrating and finding the amount of phase offset from $1A$ in the coil, the shim components can be defined as Hz/A and are found via the field map as they are the equivalent gradient for the corresponding direction. The solution of the matrix equation is therefore found by shim currents that best apply to the linear combinations for each voxel resulting in the phase offsets.

When solving matrix equations there are a few terms worth discussing. A matrix M has a property called rank, which describes the number of linearly independent rows a matrix has. This number will define the dimension which the matrix can span[23]. The basic $3x3$ identity matrix will have three linearly independent rows/columns and therefore have $rank(M) = 3$.

$$
\begin{bmatrix} 1 & 0 & 0 \\ 0 & 1 & 0 \\ 0 & 0 & 1 \end{bmatrix}
$$

When solving a matrix equation, the rank can be used to determine if it is possible to find a unique solution. When the rank of the matrix is equal to the number of variables, this is possible. The following matrix has a rank of 2 with two variables and would solve for $a = 2$ and $b = 1$.

$$
\begin{bmatrix} 7 \\ 9 \end{bmatrix} = \begin{bmatrix} 2 & 3 \\ 3 & 3 \end{bmatrix} \cdot \begin{bmatrix} a \\ b \end{bmatrix}
$$

In the case of solving the matrix equation for shim currents in a slice, the rank is probably far larger than than the number of shim channels. In that case, we will have an overdetermined system and there will not be a solution that solves the equation. The solution is instead an estimate to solve Ax as close to b as possible. The amount of error related to the estimate is determined by how well-conditioned it is. A well-conditioned problem is defined as when small changes in the data b produce small changes in the solution x. In the same case, an ill-conditioned problem will produce large changes in the solution[24].

To create a matrix as well-conditioned as possible, the shim calculation utilizes the neighbouring voxels to determine the shim components. To achieve this a slab width is defined which spans the current voxel and neighbours within the slab width. The purpose of this is to determine the gradient in the voxel with information of its neighbour to better estimate the shim currents for the slice. Figure A.1 shows how in the z-direction, multiple slices can be included to calculate the gradient within the current slice. Since field maps favour a smooth trend, a wider slab width will use the information from the neighbours in the estimation to take this into account.
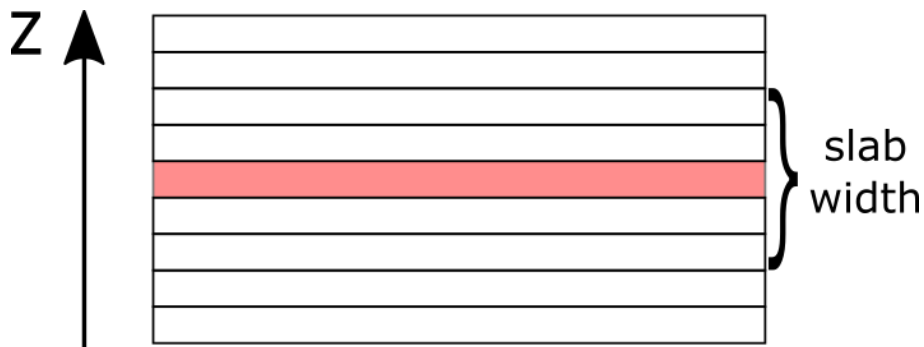

Figure A.1: Illustration of the slab width in the z-direction where neighbouring slices are used to determine the gradient for the calculation of shim values in the current slice (shown in red).

The choice of slab width introduces a trade-off, as by increasing the slab width, more information is included in the calculation. This reduces the noise present in the field map, but at the same time reduces the localization of each voxel. As more voxels are included in the estimation of the gradient in one voxel, the weighting of the gradient inside the voxel itself will be reduced. In turn, this could ensure that for a periodic pattern over an area it can lose its defining features as the slab width not only reduces the noise but also encompasses too many voxels and the peaks in the pattern are diminished. This means the choice of slab width is not as simple as choosing the highest value available will give the best results. At a point, the accuracy of the calculation will degrade as the voxels lose their localization. A well-conditioned matrix in this problem is therefore defined by a slab width able to reduce the amount of noise necessary without losing to much of the periodic pattern present in the spinal cord.

B Additional figures and tables

Slice	$S_x(\mu T/m)$	$S_y(\mu T/m)$	$S_z(\mu T/m)$	$\Delta\omega$ (Hz)
1	-17.8	3.5	106.3	172.0
2	-15.9	4.9	143.7	97.4
3	-18.3	5.0	140.6	99.2
4	-18.8	4.3	147.6	93.2
5	-18.4	3.2	155.5	90.9
6	-17.7	3.0	152.6	92.7
7	-17.3	3.8	167.6	97.4
8	-15.9	5.1	170.8	100.8
9	-13.4	7.0	166.5	96.5
10	10.2	6.8	173.0	106.6
11	6.4	8.0	178.8	114.0

Table B.1: Numerical calculation results for the shim values and the frequency offset from the 1st-order Z-inhomogeneity with an offset of -150 $\mu T/m$.

Slice	$S_x(\mu T/m)$	$S_y(\mu T/m)$	$S_z(\mu T/m)$	$\Delta\omega$ (Hz)
1	-112.1	3.6	28.0	53.4
2	-116.1	5.7	6.9	103.5
3	-119.3	6.3	0.13	113.0
4	-115.4	5.3	21.5	92.3
5	-109.1	4.3	45.3	85.6
6	-107.0	2.9	41.1	102.5
7	-101.0	3.5	-4.9	91.5
8	-111.2	5.9	20.0	110.8
9	-114.3	7.4	23.0	117.8
10	-111.5	7.9	35.2	137.0
11	-107.4	9.3	40.8	146.3

Table B.2: Numerical calculation results for the shim values and the frequency offset from the 1st-order X-inhomogeneity with an offset of 100 $\mu T/m$.

Figure B.1: Calculation results from the 1st-order X-inhomogeneity with an offset of 100 $\mu T/m$. The graphs show the B_0 offset field and the shim values for the 1st-order shim coils. The red stars indicate the slice positions of the image to be compensated.

Slice	$S_x(\mu T/m)$	$S_y(\mu T/m)$	$S_z(\mu T/m)$	$\Delta\omega$ (Hz)
1	-17.1	53.0	-19.5	22.5
2	-15.5	54.9	0.94	-11.4
3	-18.3	55.4	5.0	-7.2
4	-18.6	54.8	-1.8	-8.2
5	-18.1	53.7	4.2	-10.0
6	-17.6	53.4	4.7	-8.7
7	-17.2	54.1	13.6	-6.2
8	-15.9	55.7	12.8	-8.1
9	-13.6	57.2	19.5	-1.6
10	-10.8	57.1	28.5	13.2
11	-7.1	58.3	29.7	12.1

Table B.3: Numerical calculation results for the shim values and the frequency offset from the 1st order Y-inhomogeneity with an offset of -50 $\mu T/m$.
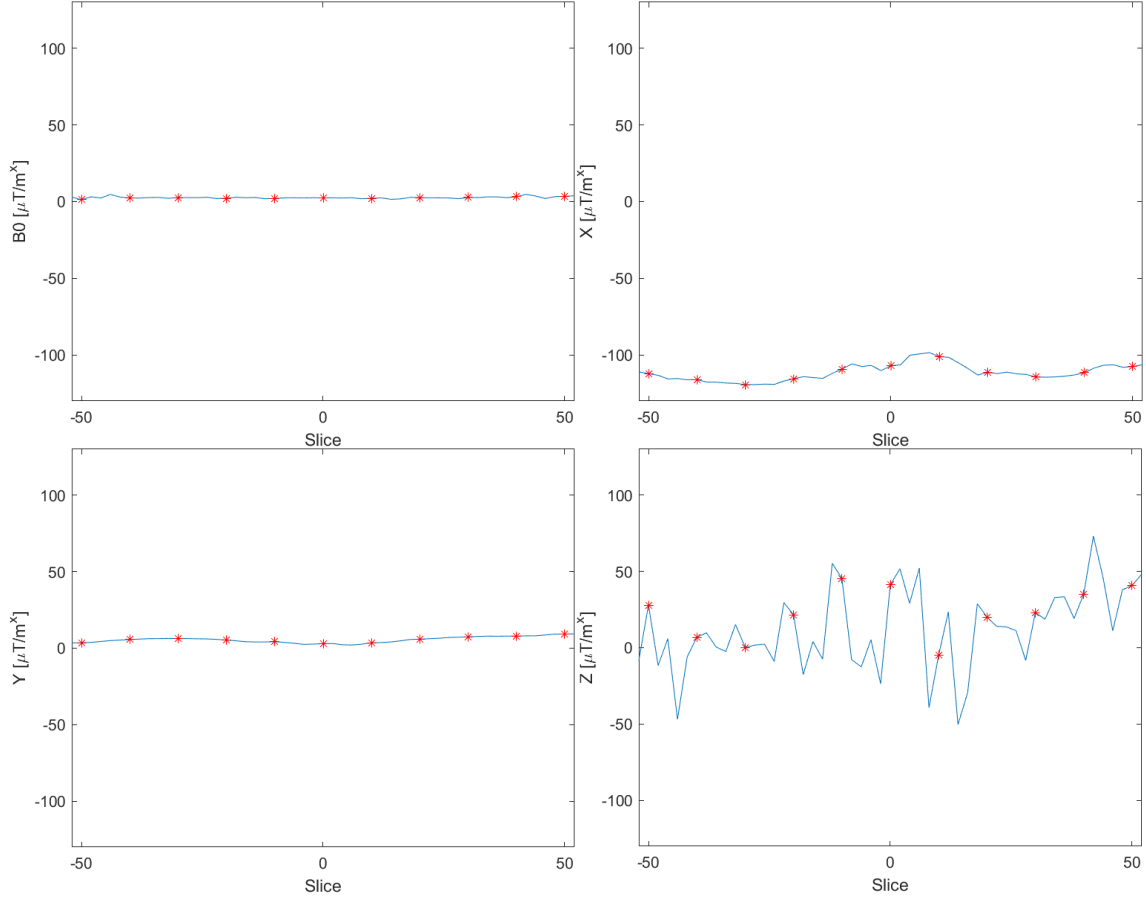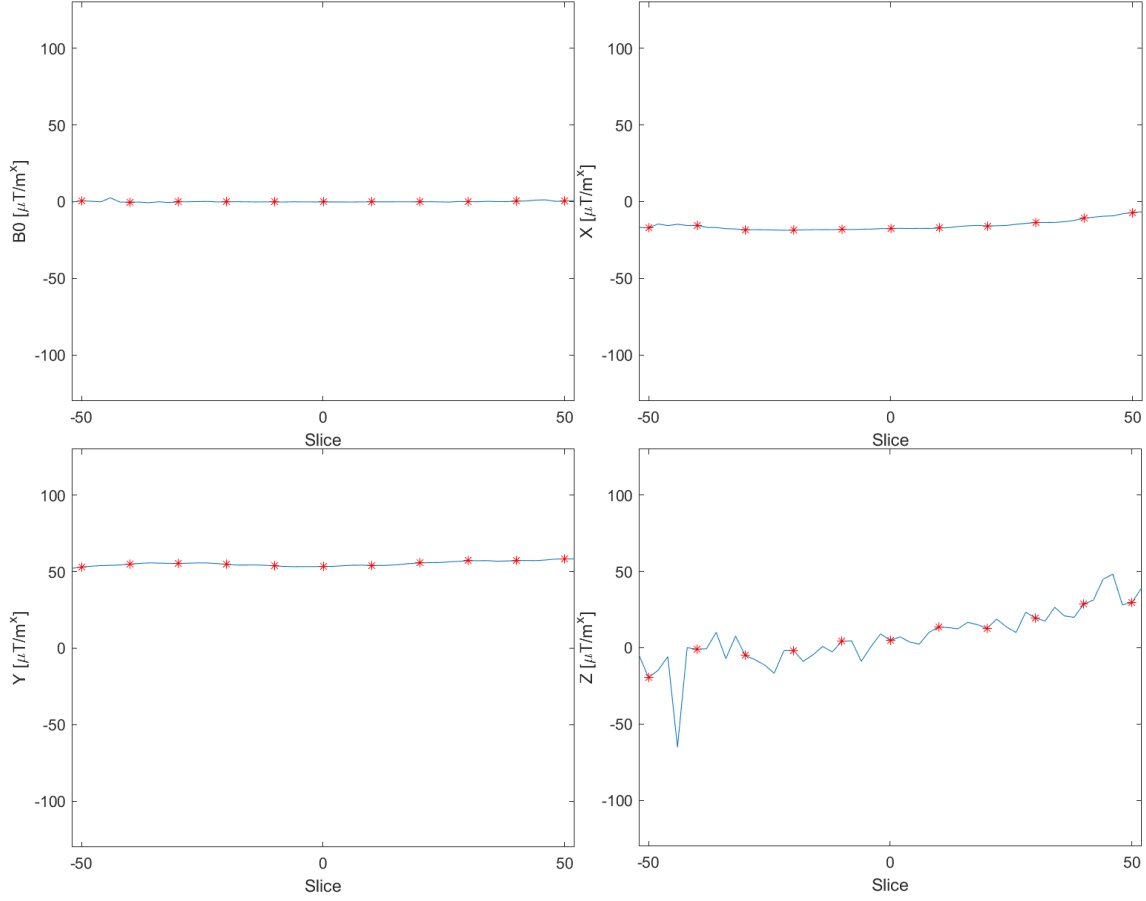
Figure B.2: Calculation results from the 1st-order Y-inhomogeneity with an offset of -50 $\mu T/m$. The graphs show the B_0 offset field and the shim values for the 1st-order shim coils. The red stars indicate the slice positions of the image to be compensated.

Slice	$S_x(\mu T/m)$	$S_y(\mu T/m)$	$S_z(\mu T/m)$	$\Delta\omega$ (Hz)
1	30.2	3.28	-29.4	77.0
2	22.1	487	4.41	30.0
3	9.83	5.58	7.55	33.4
4	-0.012	46.4	1.51	30.1
5	-9.23	3.87	1.70	30.8
6	-18.3	3.47	0.020	31.47
7	-27.5	4.10	13.0	33.7
8	-35.8	5.77	16.2	35.0
9	-43.2	7.40	18.2	35.5
10	-50.4	7.55	32.6	57.7
11	-56.3	8.84	37.6	65.5

Table B.4: Numerical calculation results for the shim values and the frequency offset from the 2nd order ZX-inhomogeneity with an offset of 500 $\mu T/m^2$.
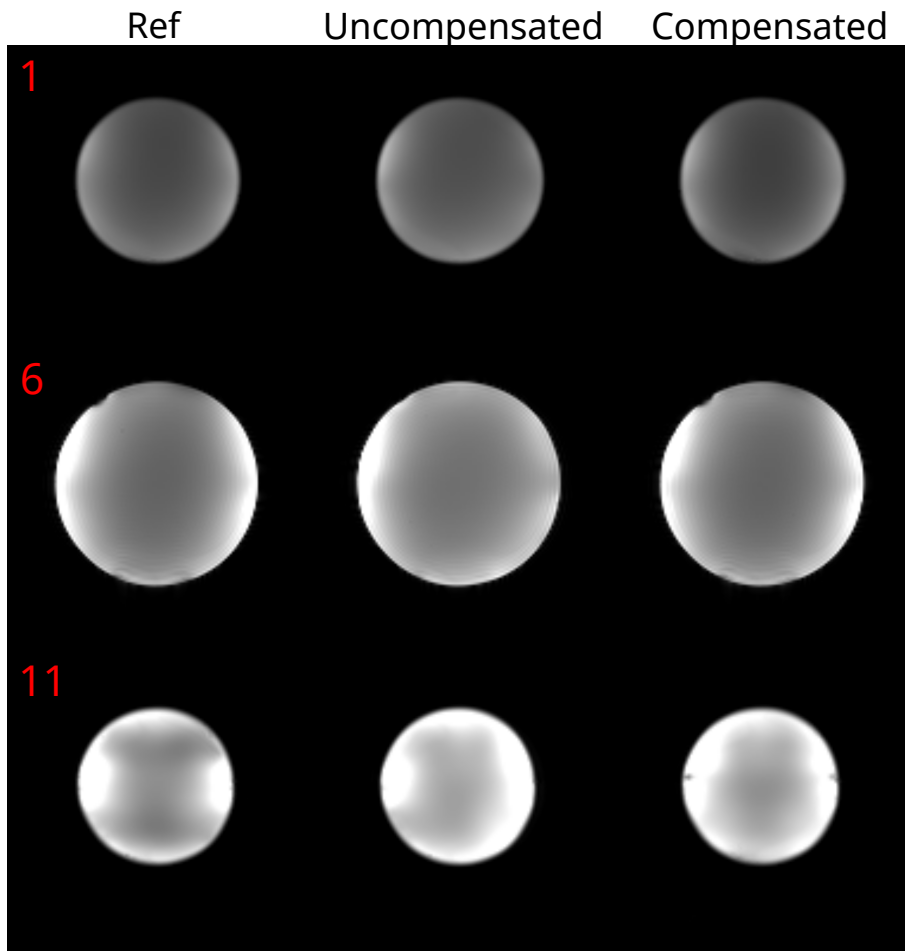
Figure B.3: Slices 1, 6 and 11 of the measurement using a 1st-order Y-inhomogeneity of -50 $\mu T/m$ with and without shim compensation as well as a reference measurement. The images is from the signal at the ninth echo which had an echo time of 34.97 ms.
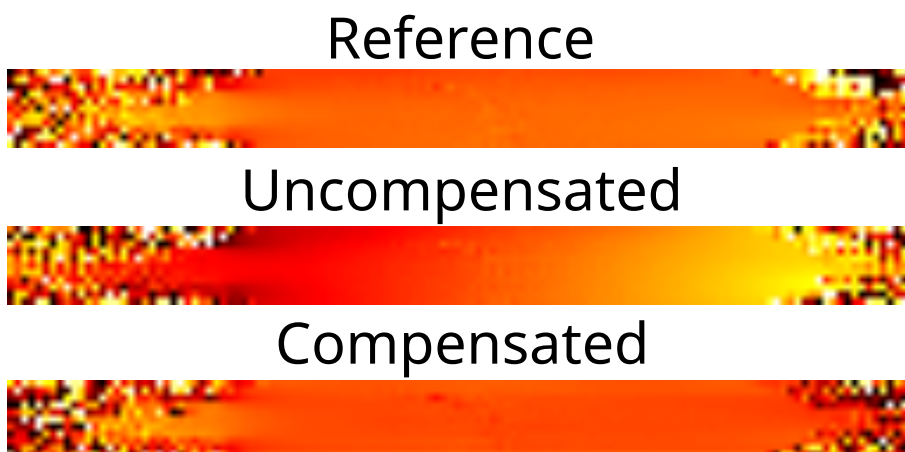

Figure B.4: Field maps from 1st-order Y-inhomogeneitiy measurements. Shown in the sagittal plane.

Slice	$S_x(\mu T/m)$	$S_y(\mu T/m)$	$S_z(\mu T/m)$	$\Delta\omega$ (Hz)
1	-12.3	-259.9	-625.7	1177.9
2	6.8	-197.6	-33.9	86.1
3	-0.58	-151.3	49.9	-20.2
4	14.4	-78.6	-528.8	867.9
5	-2.6	25.5	-230.8	583.4
6	-16.4	35.7	184.7	137.0
7	-19.7	1.4	225.3	76.1
8	-19.8	-11.5	103.2	152.8
9	-17.9	-9.2	75.3	167.4
10	-17.6	-4.8	86.8	165.9
11	-17.0	-4.3	115.0	165.9
12	-16.1	-5.8	124.4	169.5
13	-15.0	-7.2	96.1	157.9
14	-14.3	-7.5	112.4	168.1
15	-12.8	-6.5	107.9	163.4
16	-10.9	-5.5	102.2	155.2
17	-10.1	-3.3	124.6	182.8
18	-10.7	-0.80	105.1	154.6
19	-10.7	4.0	100.9	146.3
20	-12.5	5.9	84.0	111.3

Table B.5: Numerical calculation results for the shim values and the frequency offset from in vivo field map with tune-up only.

Slice	$S_x(\mu T/m)$	$S_y(\mu T/m)$	$S_z(\mu T/m)$	$\Delta\omega$ (Hz)
1	10.5	37.7	58.4	14.5
2	5.1	40.2	-53.3	233.5
3	2.7	44.4	49.1	60.2
4	-12.1	4.3	11.9	-35.2
5	-21.5	34.8	43.3	49.9
6	-22.6	22.5	81.0	7.3
7	-22.5	3.7	88.3	-9.8
8	-22.5	-16.1	85.9	-20.2
9	-20.4	-15.2	-32.6	36.0
10	-20.7	-7.2	-26.0	35.2
11	-21.6	-0.29	-0.51	36.4
12	-21.7	-4.2	21.7	38.5
13	-21.5	-6.7	19.4	37.0
14	-20.9	-7.1	7.5	30.4
15	-20.8	-7.2	17.9	38.2
16	-19.5	-5.9	22.4	41.6
17	-18.0	-3.6	28.4	49.1
18	-17.6	-1.7	5.2	13.7
19	-16.8	1.7	11.3	21.5
20	-18.1	4.9	29.7	57.0

Table B.6: Numerical calculation results for the shim values and the frequency offset from in vivo field map with static shim applied.